

ABSTRACT

Title of Dissertation: **BENZOCYCLOBUTENE MICRORING
RESONATORS**

Wei-Yen Chen, Doctor of Philosophy, 2007

Dissertation Directed By: **Professor Ping-Tong Ho
Department of Electrical and Computer
Engineering**

Wavelength division multiplexing (WDM) at optical carrier frequencies offers more capacity and flexibility of fiber networks and upgrades conventional point-to-point fiber-optic transmission links to multiuser networks for the demand of high-speed network systems. The microring resonator, which has been seen in action in many photonic devices, is ideal for WDM applications in realization of narrow bandwidth with a wide free spectral range.

In this research, microring resonators are fabricated in benzocyclobutene (BCB), a popular polymer in photonics and electronics applications. First, the single-mode BCB undercut-cladding waveguides were designed to reduce bending loss. BCB microring resonators were fabricated based on those principles. BCB single-microring devices were demonstrated as add-drop filters and notch filters with a negative coupling gap. Not only are the microring resonators compact (as small as 5

μm in radius) for photonic VLSI, they also exhibit a high out-of-band rejection (~ 30 dB), high extinction as well as a high finesse (~ 285).

In addition, BCB lattices consisting of over one hundred microring resonators were fabricated and demonstrated as bandstop filters. The lattices, despite the large number of resonators, exhibit an extremely low propagation loss. Finally, optical bistability and the field-enhanced all-optical nonlinear switching were demonstrated in BCB microring devices.

BENZOCYCLOBUTENE MICRORING RESONATORS

By

Wei-Yen Chen

Dissertation submitted to the Faculty of the Graduate School of the
University of Maryland, College Park, in partial fulfillment
of the requirements for the degree of
Doctor of Philosophy
2007

Advisory Committee:
Professor Ping-Tong Ho, Chair
Professor Emeritus Chi H. Lee
Professor Shihab Shamma
Professor Wendell T. Hill III
Dr. Warren N. Herman

© Copyright by
Wei-Yen Chen
2007

DEDICATION

To my parents,

Tsong-Maw Chen and Hsin-Chien Chang.

ACKNOWLEDGEMENTS

I would like to express my appreciation and gratitude to my advisor, Professor Ping-Tong Ho, for his guidance and support in my study and research. His insight and experience in photonics has helped me to understand this field. His patience and care has been comforting and encouraging.

I am also grateful to my coworkers in the same lab: Dr. Vien Van gave me a theoretical background as well as a practical implementation on microring resonators, Tie Nan Ding supported my research with simulations. Dr. Tarek Ibrahim, Dr. Rohit Grover, and Dr. Kuldeep Amarnath helped me in fabrication and device testing.

The collaboration with Professor Chi H. Lee's group was inspiring. I received his generous support in experimental facilities as well as many research ideas. Dr. Weiluo Cao instructed me on nonlinear experiments in microrings. Min Du shared her experiences in clean room, which saved me from futile trials.

I appreciate Professor Goldhar for fruitful discussions and generous sharing of experimental equipments. Also, I would like to thank Professor Shihab Shamma and Professor Wendell T. Hill III for reading and commenting on my thesis.

I would like to thank Dr. Warren Herman, the project leader of the polymer group at the Laboratory for Physical Sciences (LPS), for displaying a promising picture in polymer-photonics research. In addition, I sincerely appreciate his patient and careful reading of my papers and correcting my English. I also extend my gratitude to Dr. Marshall Saylor, Dr. Ken Ritter, Dr. Norman Moulton, Bernadette Preston, and William Klomprens, whose efforts and leadership made LPS among one of top research facilities.

I will not forget all the technical supports from the LPS staff: Toby Olver, Bob Klause, Scott Horst, Steve Brown, Dan Hinkel, Lisa Lucas, Sal Martinez, Mike Khbeis, Suzanne Fritz, Dr. William Johnson, J.B. Dottellis, Russell Frizzell, Butch Bilger, Greg Latini, Mark Thornton, Jeff McKinney, Michael Anders, Eugene Cszaszar, Catherine Barcey Tynes, Julie Woody, Cynthia Evans, and Sandy Gloria. Also my colleagues at LPS: Li-Chiang Kuo, Dr. Shuo-Yen Tseng, Dr. Yongzhang Leng, Victor Yun, Yi-Hsing Peng, Dong Hun Park, and Dr. Younggu Kim. My days at LPS would have been miserable and endless without their help.

Last but not the least, I would like to thank all communities of the University of Maryland. My studies here have not only provided me with a foundation for research, but have also broadened my views on a real and diversified world. All the friends here have made my life more colorful and fruitful.

Table of Contents

DEDICATION.....	ii
ACKNOWLEDGEMENTS.....	iii
Table of Contents.....	v
List of Tables.....	ix
List of Figures.....	x
Chapter 1 Introduction.....	1
1.1 Motivation.....	1
1.1.1 Microring Resonators as Key Components in WDM Systems.....	2
1.1.2 Microring Resonators in Polymers.....	3
1.1.3 Microring Resonators in Benzocyclobutene.....	5
1.2 Research Objectives.....	6
1.3 Scope of the Thesis.....	6
Chapter 2 Theoretical Overview on Microring Resonators.....	7
2.1 Introduction.....	7
2.2 Coupling and Transmission Strength.....	7
2.3 All-Pass Configuration.....	11
2.4 Add-Drop Configuration.....	14
2.5 Characteristics of Microring Resonators.....	15
2.5.1 Field Enhancement.....	15
2.5.2 Free Spectral Range.....	18
2.5.3 Bandwidth.....	18

2.5.4	Finesse.....	20
2.5.5	Cavity Lifetime	22
2.5.6	Quality Factor	22
Chapter 3	Design and Fabrication of BCB Microring Resonators	24
3.1	Introduction.....	24
3.2	Optical Design of BCB Waveguides and Microring Resonators.....	24
3.2.1	Layer Structure.....	24
3.2.2	Single-Mode Operation.....	25
3.2.3	Coupling Constant and Coupling Strength	26
3.2.4	Propagation Loss.....	27
3.3	Fabrication Steps.....	32
3.3.1	Sample Preparation	32
3.3.2	SiO ₂ Deposition	36
3.3.3	BCB Deposition.....	36
3.3.4	Photolithography.....	36
3.3.5	Etch-mask Deposition.....	36
3.3.6	Pattern Transfer.....	38
3.3.7	Anisotropic Dry-Etching.....	38
3.3.8	Etch-Mask Removal.....	38
3.3.9	Sample Cleaving	39
3.3.10	Isotropic Wet-Etching.....	39
Chapter 4	Single-Microring Devices.....	41
4.1	Introduction.....	41

4.2	Add-Drop Filters	41
4.2.1	High-Extinction and High-Out-of-Band-Rejection Racetrack	41
4.2.2	Compact, Wide-FSR, and High-Finesse Microrings	44
4.3	Notch Filters.....	47
4.3.1	Ultra-Compact Microring Notch Filter	47
4.3.2	Negative-Gap Microring Notch Filters	49
4.4	Conclusions.....	54
Chapter 5	Microring Lattices.....	55
5.1	Introduction.....	55
5.2	Theory	56
5.3	Device Characteristics	61
5.4	Conclusions.....	65
Chapter 6	Nonlinear Effects in Microring Resonators	67
6.1	Introduction.....	67
6.2	Thermal Tuning	68
6.3	Optical Bistability in Single Microring Resonator	68
6.3.1	Theory	68
6.3.2	Experiment.....	70
6.3.3	Mechanism for Optical Bistability in BCB Microring Resonators.....	73
6.4	All-Optical Nonlinear Switching in Microring Lattice.....	75
6.4.1	Analysis on Field Enhancement Factor	76
6.4.2	Experiment.....	81
6.5	Conclusions.....	85

Chapter 7	Conclusions.....	87
7.1	Achievements.....	87
7.2	Future Directions	87
Appendix A	Field Enhancement Factor in Lossless Microring Resonators.....	89
Bibliography	91

List of Tables

Table 1.1:	Comparison of various materials for microring devices.....	5
------------	--	---

List of Figures

Figure 2.1:	Schematic diagram of a microring resonator in all-pass configuration.	8
Figure 2.2:	Schematic diagram of a two-port system in a microring resonator. Both the input and output fields contain one field in the microring and the other in the straight bus waveguide.	9
Figure 2.3:	Phase shift of a lossless microring resonator.	12
Figure 2.4:	The intensity at the through port with a fixed round-trip amplitude a_{rt} and different transmission strength τ . a_{rt} used here is 0.8.	13
Figure 2.5:	Schematic diagram of a microring resonator in add-drop configuration.	15
Figure 2.6:	The intensity at the through port and the drop port with a fixed round-trip amplitude a_{rt} and different coupling strength τ . a_{rt} used here is 0.95.	16
Figure 2.7:	The field enhancement of a microring resonator (a) in all-pass configuration; (b) in add-drop configuration.	17
Figure 2.8:	The finesse of a microring resonator (a) in all-pass configuration; (b) in add-drop configuration.	21
Figure 3.1:	Schematic diagram of a BCB channel waveguide.	25
Figure 3.2:	Schematic diagram of a microracetrack resonator.	28
Figure 3.3:	Schematic diagram of a BCB undercut channel waveguide.	29

Figure 3.4:	The optical intensity distribution of a bent BCB waveguide (a) in regular scheme, (b) in channel-waveguide scheme, (c) in undercut-channel-waveguide scheme.	30
Figure 3.5:	Simulated round-trip amplitude of a BCB microring resonator with a core of $1.8 \mu\text{m} \times 1.8 \mu\text{m}$ and a bent radius of $10 \mu\text{m}$	31
Figure 3.6:	The optical intensity distribution (a) in the straight section and (b) in the curved section of a BCB microracetrack. The curved section has a radius of $10 \mu\text{m}$	32
Figure 3.7:	Process flow for BCB microring resonators: (a) substrate preparation, (b) SiO_2 deposition, (c) BCB deposition, (d) photoresist spin-coat, (e) photolithography, (f) aluminum deposition, (g) photoresist lift-off, (h) BCB etching, (i) SiO_2 etching, (j) aluminum removal, and (k) wet etching.....	35
Figure 3.8:	SEM image of BCB waveguides using (a) a SiO_2 etching mask; (b) an aluminum etching mask. The residue of SiO_2 cap remained on the BCB waveguide.	37
Figure 3.9:	(a) A SEM picture of a fabricated BCB microring resonator. (b) A clear coupling gap between the bus waveguide and the microring cavity.....	40
Figure 4.1:	Setup for device testing.....	42
Figure 4.2:	Measured spectral response of a BCB microracetrack at (a) the through port and (b) the drop port. The racetrack has a radius of $20 \mu\text{m}$ and a straight coupling section of $10 \mu\text{m}$	43

Figure 4.3:	(a) Drop-port response of a BCB microring with a radius of 10 μm and (b) a detail scan at the resonance wavelength in logarithm scale.	45
Figure 4.4:	(a) Optical micrograph of a BCB microring resonator with a radius of 5 μm . (b) Drop-port spectrum of the BCB device.	46
Figure 4.5:	(a) Optical micrograph of a BCB microracetrack resonator with a radius of 2.5 μm and a straight coupling section of 10 μm . (b) Measured transmission spectrum of the BCB device.	48
Figure 4.6:	Schematic diagram of a negative-gap microring resonator.	50
Figure 4.7:	A FDTD simulation on transmission response at 1550 nm of a BCB microring device with a radius of 15 μm	51
Figure 4.8:	(a) Optical micrograph of a BCB microring resonator with a radius of 15 μm and a coupling gap of -0.6 μm , and (b) its measured transmission spectrum of the BCB device.	52
Figure 4.9:	(a) Optical micrograph of a BCB microracetrack with a radius of 15 μm , a straight section of 20 μm , and a coupling gap of -0.2 μm , and (b) its measured transmission spectrum.	53
Figure 5.1:	(a) Schematic diagram of a periodic microring lattice. (b) Components of a period.	57
Figure 5.2:	Theoretical response of the lattice with 1, 10, 20, and 36 periods where the ring resonators have 1% coupling efficiency and 4% round-trip loss.	60

Figure 5.3:	Stopband width and transmission loss of the lattice with 1% coupling efficiency and 4% loss.	60
Figure 5.4:	Stopband width and transmission loss of the 36-period lattice with 4% round-trip loss.....	61
Figure 5.5:	Optical micrograph on part of a 36-period BCB microring lattice.....	63
Figure 5.6:	Calculated band diagram and the through port transmission spectrum of the device.	63
Figure 5.7:	Transmission spectrum of a 36-period microring lattice.	64
Figure 5.8:	Measured and theoretical transmission spectra of the 36-period microring lattice.	64
Figure 5.9:	Transmission spectrum of a 56-period BCB microring lattice.	65
Figure 6.1:	Measured transmission spectra of a 56-period BCB microring lattice at 15 °C and 50 °C.....	69
Figure 6.2:	Hysteresis cycle of the optical bistability in a BCB microring resonator.....	71
Figure 6.3:	Simulated transmission of the optical bistability in a microring resonator (from Dr. W. Herman).	72
Figure 6.4:	Measured drop-port power from a microring device with wavelength (a) up-tuning and (b) down-tuning.	74
Figure 6.5:	Schematic diagram of (a) a single-row microring lattice, (b) a double-row microring lattice, and (c) components in one period of a single-row and a double-row microring lattice, respectively.	77

Figure 6.6:	The dynamic field enhancement factor of a 2-period double-row microring lattice with (a) Λ equivalent to one-half of L and (b) Λ equivalent to three-quarters of L . (c) The dynamic field enhancement factor of a 2-period double-row microring lattice with Λ equivalent to one-half of L	81
Figure 6.7:	Optical micrograph of a 56-period BCB microring lattice used in the experiment.....	82
Figure 6.8:	Experimental setup for pump-and-probe method.	82
Figure 6.9:	Measured response of probe signal.....	84
Figure 6.10:	Theoretical dynamic FE of the rings in a 56-period double-row microring lattice.	84
Figure 6.11:	The FE of the microrings after cavity charging time and at the maximum. Microrings in the 31 st period and after are neglected because of their little contribution to the switching.....	85

Chapter 1

Introduction

1.1 Motivation

The twenty-first century witnesses an explosion of data-traffic volume, as the demand of high-speed multimedia services on mobile phones, television networks, and internet keeps growing day by day. The solution for overloading issues on traditional telecommunications is to utilize wavelength-division multiplexing (WDM), a technology modulating multiple baseband signals on optical carrier frequencies.

WDM offers the potential of increasing the capacity and flexibility of fiber networks and upgrading conventional point-to-point fiber-optic transmission links to multiuser networks. High optical carrier frequencies of WDM systems provide a thousand times more available channels than current telecommunication facilities. In addition, WDM systems experience no crosstalk, as independent optical information with different wavelengths can be combined, routed, switched, and separated without interference from one another. Most importantly, fiber-optics, the platform performing WDM, features exceptionally low loss over long distance, reducing the numbers and the cost of repeaters or amplifiers. In particular, the advent of erbium-doped fiber amplifier (EDFA) operating within C band (1550-nm window) directly amplifies optical signals without having to convert the signals into the electrical

domain, increasing the speed of the whole system and decreasing the need for extra converters.

1.1.1 Microring Resonators as Key Components in WDM Systems

Implementation of WDM networks requires a variety of passive and active devices, such as couplers, filters, multiplexers, demultiplexers, and optical amplifiers [1]. In order to meet the requirements of the current network market, the speed of WDM devices has to be high. In addition, from an economical prospective, reducing cost in fabricating, integrating, and maintaining WDM devices and systems is required to attract more users and to create potential business opportunities.

The optical ring resonator was first proposed in the late 1960s [2], and its radius varied from the order of meters to micrometers [3]–[6]. The microring resonator, with a radius on the order of micrometers, is an ideal candidate for WDM applications in realization of narrow bandwidth with a wide free spectral range (FSR). Microring resonators have been used in some photonic devices such as channel dropping filters [7], WDM demultiplexers [8], and true ON–OFF switches [9], light-emitting diodes (LEDs) [10]. Other than photonics, microring devices have also been employed in other scientific and engineering applications such as biochemical sensing and ultrasound detection [11]–[12].

Furthermore, microring devices can be as compact as a few micro radii, so integrating as many as 10^5 microring devices per square centimeter becomes feasible for very large scale integrated (VLSI) photonic circuits in WDM systems [13]. Thanks to their compact size, the speed of the microring devices can be as fast as picoseconds.

1.1.2 Microring Resonators in Polymers

Microring resonators have been designed and fabricated with various materials [6],[14]–[19]. Among all available materials, semiconductors have been most popularly used in microring technology because of their well-developed fabrication processing. Semiconductor microring devices can be ultra-compact because of their negligible bending loss resulting from high refractive-index contrast [6]. High optical nonlinearity of some semiconductors makes devices with active control and devices for all-optical signal processing feasible. However, the scattering loss of semiconductors, which is determined by surface roughness and the refractive index of the material, is as huge as 20 dB/cm [20]. In addition, modal mismatch and coupling loss between the fiber and tightly confined semiconductor waveguide remains high regardless of the anti-reflection coatings applied at the waveguide facets. Epitaxial growth in semiconductor fabrication is a complicated and time-consuming process, and the equipment required for the process is complex and expensive.

Compared with semiconductors, silica-based material features extremely low propagation loss and a simpler fabrication processing. In addition, the refractive index of silica can be tuned by different deposition recipes. Nevertheless, low optical nonlinearity of silica-based material restricts its use to passive-device application in integrated photonic circuits. Even though the optical nonlinearity of silica can be improved 8 times by impurity doping, the doping results in 1000 times larger loss, making this idea non-profitable [21]–[22].

The emergence of polymers provides a novel solution. Low-loss polymers with different refractive indices have been developed and drawn attention because of their cost-effective aspect [23]–[24]. Although polymers with C–H bond vibrations exhibit material absorption at the wavelength of 1550 nm, this absorption can be significantly reduced by employing fluorinated or deuterated polymers [25]. Not only can the low refractive-index polymers reduce the scattering loss from waveguide roughness, they also increase the coupling efficiency between waveguides, providing a looser processing requirement on coupling gaps. In view of device fabrication, a variety of simple fabrication techniques are available for polymer processing: photolithography [26], soft lithography replica molding [27], imprinting [28], photobleaching [29], and multiphoton absorption polymerization [30], just to name a few. Finally, polymers are promising materials for the realization of active and nonlinear microring devices because of their large nonlinear optical effects [31]–[33]. The advantages and disadvantages of each material are summarized in Table 1.1.

Only a few polymer ring devices were demonstrated at the inception of my research topic. The first polymer ring resonator was fabricated in rhodamine 6G doped polyurethane [5]. The device, demonstrated as a thin-film ring laser, consisted of a 5-mm diameter glass rod coated with the polymer for a resonator circumference of 31.4 mm. A multi-mode polymer ring resonator was fabricated by the photopolymerization of doped polymethyl methacrylate films [4]. It is not surprising that the propagation loss was low because the radius of the ring resonator was 4.5 cm. Not until recently were integrated optical polymer ring resonators demonstrated [34]. The devices were demonstrated passively as filters and actively as electrooptic

Table 1.1: Comparison of various materials for microring devices.

Material	Advantages	Disadvantages
Semiconductors	<ul style="list-style-type: none"> • Well-developed fabrication • Ultra-compact devices • High optical nonlinearity 	<ul style="list-style-type: none"> • Complex processing steps • High cost on equipments • High propagation loss
Silica	<ul style="list-style-type: none"> • Simple fabrication steps • Low propagation loss 	<ul style="list-style-type: none"> • Low optical nonlinearity • Limited photonic circuit applications
Polymers	<ul style="list-style-type: none"> • Various fabrication techniques • Simple fabrication steps • Low propagation loss • High optical nonlinearity 	<ul style="list-style-type: none"> • Not fully mature processing steps

modulators; however, the radii of the rings were on the order of hundred μm so the dimension of the devices were still large.

1.1.3 Microring Resonators in Benzocyclobutene

Benzocyclobutene (BCB) was chosen for microring-resonator applications in this work. Because of its attractive material properties, such as high degree of planarization, low moisture absorption, high chemical resistance, high thermal

stability, low dielectric constant (which lowers the refractive-index difference at the coupling gap, increases the coupling strength and hence reduces fabrication difficulties), high optical clarity, and low optical absorption loss [35]–[36], BCB has become a popular polymer for photonics and electronics applications such as optical waveguides and wafer bonding [37]–[38]. The nonlinear optical properties of BCB were; however, unavailable, and direct study of BCB on microring resonators was never reported.

1.2 Research Objectives

The goal and novelty of this work is to fabricate compact, single-mode BCB microring resonators at 1550-nm window and demonstrate their use in photonics applications.

1.3 Scope of the Thesis

This chapter has given an introduction for this research and the history of microring resonators. Chapter 2 reviews the fundamentals of microring resonators. The optical design and fabrication of BCB microring resonators is discussed in chapter 3. Chapter 4 and 5 present single-microring devices and multiple-microring devices, or microring lattices, respectively. Chapter 6 demonstrates nonlinear effects and all-optical nonlinear switching of microring devices. Finally, chapter 7 summarizes the accomplishments of this dissertation and suggests a perspective of future works.

Chapter 2

Theoretical Overview on Microring Resonators

2.1 Introduction

A microring resonator is a ring-shaped waveguide, as shown in Fig. 2.1, whose radius ranges from microns to hundred microns. Light can be coupled into or out of the resonator from or to another nearby waveguides by the evanescent wave. In this closed loop ring waveguide only certain wavelengths can resonate and build up their intensity. The free space resonant wavelengths λ_m are determined by

$$m\lambda_m = Ln_{eff}. \quad (2.1)$$

where m is the longitudinal mode number, L and n_{eff} are the circumference and the effective refractive index of the ring resonator, respectively.

2.2 Coupling and Transmission Strength

The microring resonator can be regarded as a two-port network. The input fields \mathbf{E}_I are on the left and the output fields \mathbf{E}_O are on the right, as shown in Fig. 2.2. Relations between the output fields to the input fields can be written as [39]

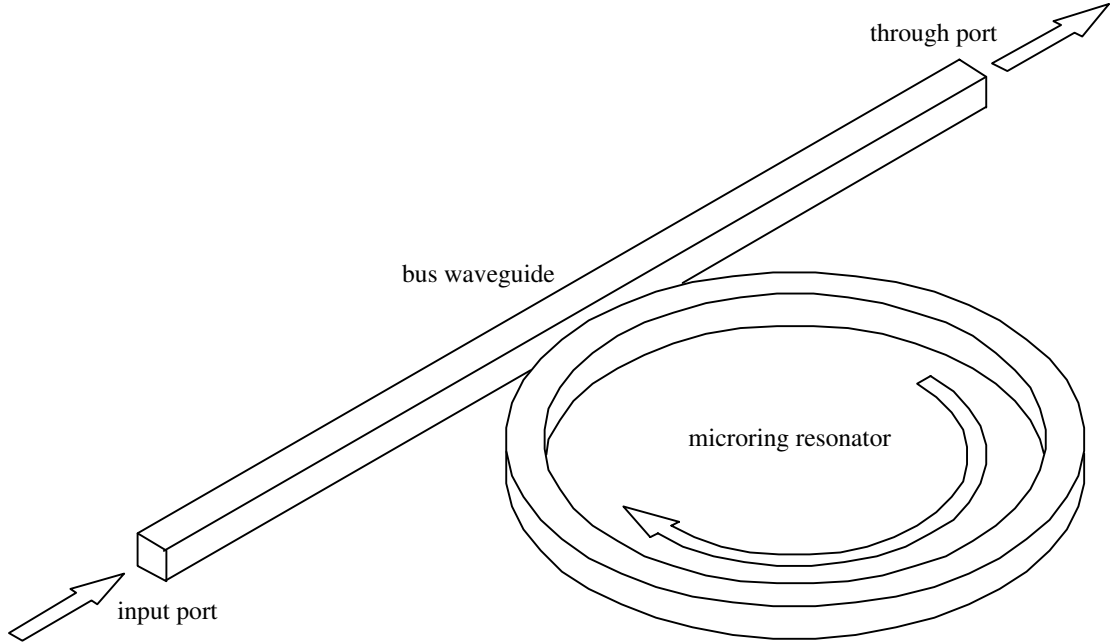


Figure 2.1: Schematic diagram of a microring resonator in all-pass configuration.

$$E_o = SE_I \quad (2.2)$$

where S is a 2×2 scattering matrix. If the system is lossless, the power conservation requires the total input power is equal to the total output power [39]

$$E_I^+ E_I = E_o^+ E_o = (SE_I)^+ (SE_I) = E_I^+ (S^+ S) E_I. \quad (2.3)$$

Therefore

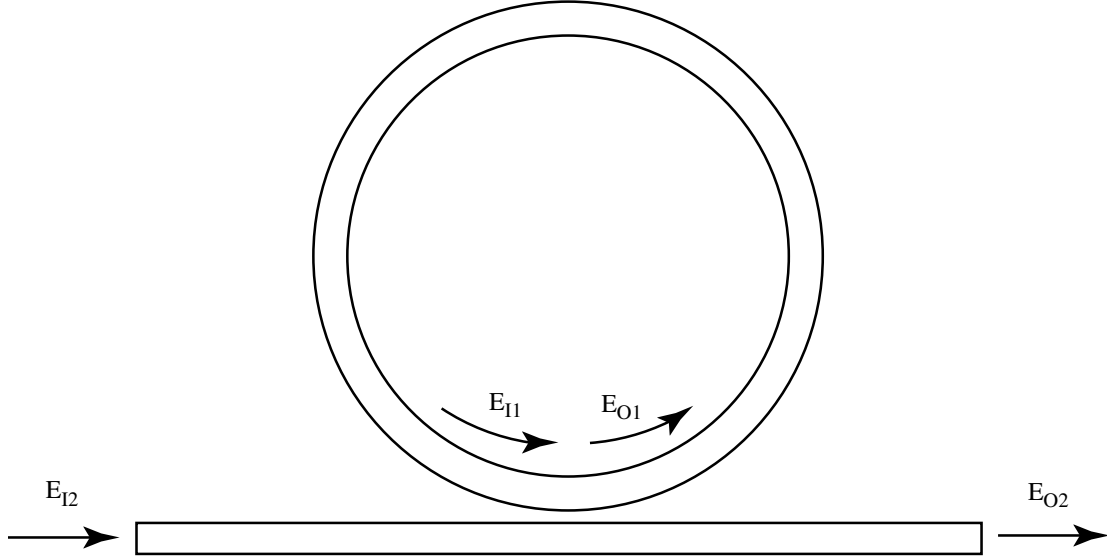


Figure 2.2: Schematic diagram of a two-port system in a microring resonator. Both the input and output fields contain one field in the microring and the other in the straight bus waveguide.

$$S^+ S = I, \quad (2.4)$$

where I is the identity matrix. In other words, S is a unitary matrix.

The property of time reversibility of light propagation in the microring leads to

$$E_I^* = S E_O^*, \quad (2.5)$$

where \mathbf{E}_I and \mathbf{E}_O are time-reversed fields. Eq. (2.5) can be rewritten as

$$E_o = (S^{-1})^* E_I. \quad (2.6)$$

Combining Eq. (2.2), (2.4), and (2.6) yields

$$S^{-1} = S^* = S^+ \quad (2.7)$$

so S is a symmetric matrix and its off-diagonal elements s_{12} and s_{21} are equal.

Assuming the coupling length is negligible, the fields would refrain the same phase while propagating from the input to the output. Therefore, the diagonal elements s_{11} and s_{22} are real numbers and the scattering matrix S can be written as

$$S = \begin{bmatrix} \tau & -j\kappa \\ -j\kappa & \tau \end{bmatrix} \quad (2.8)$$

where τ and κ are the real-number transmission and coupling strength, respectively, whereby meeting the power conservation

$$\tau^2 + \kappa^2 = 1. \quad (2.9)$$

τ^2 and κ^2 are sometimes referred to as transmission and coupling efficiency, respectively.

2.3 All-Pass Configuration

In Fig. 2.2, the circulating field inside the microring resonator \mathbf{E}_{I1} can be written as

$$E_{I1}(t) = a_{rt} E_{O1}(t - n_{eff} L / c) = a_{rt} e^{-j\phi} E_{O1}(t), \quad (2.10)$$

where a_{rt} is the round-trip amplitude and ϕ is the wavelength-dependent phase contribution in the ring resonators, respectively. ϕ is given by

$$\phi = \frac{\omega}{c} n_{eff} L = \frac{2\pi}{\lambda} n_{eff} L. \quad (2.11)$$

The circulating field inside the microring resonator \mathbf{E}_{O1} is given by

$$E_{O1}(t) = -j\kappa E_{I2}(t) + \tau E_{I1}(t) = -j\kappa E_{I2}(t) + \tau a_{rt} e^{-j\phi} E_{O1}(t), \quad (2.12)$$

The transmitted field \mathbf{E}_{O2} is given by

$$E_{O2}(t) = \tau E_{I2}(t) - j\kappa a_{rt} e^{-j\phi} E_{O1}(t). \quad (2.13)$$

At steady state, the transfer function T_{ap} can be obtained by solving Eqs (2.12) and (2.13)

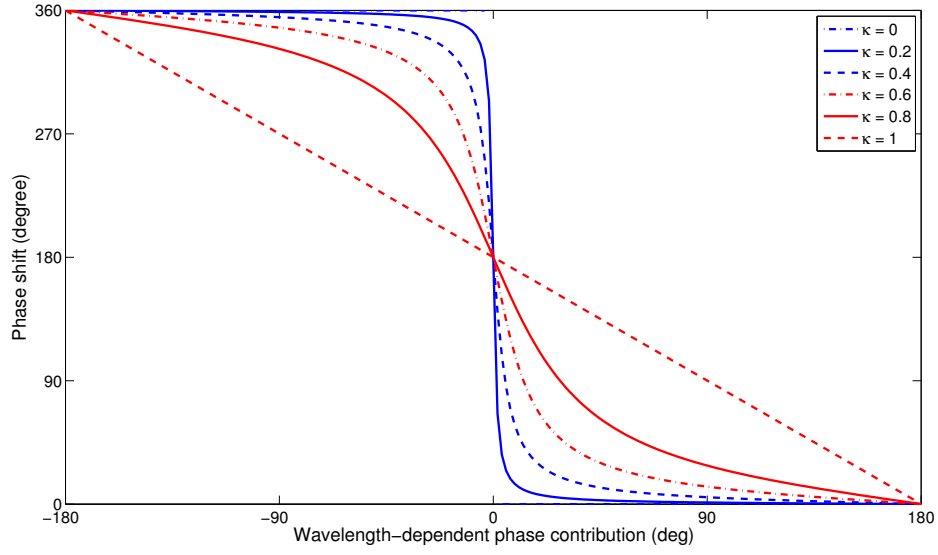


Figure 2.3: Phase shift of a lossless microring resonator.

$$T_{ap} \equiv \frac{E_{O2}}{E_{I2}} = \frac{\tau - a_r e^{-j\phi}}{1 - \tau a_r e^{-j\phi}}. \quad (2.14)$$

For a lossless microring resonator, the transfer function T_{ap} satisfies energy conservation and its magnitude is 1 regardless of phase contribution ϕ , and the microring resonator behaves as an all-pass filter. In addition, the phase shift of the transmitted field Φ is given by [40]

$$\Phi = \pi - \phi - 2 \tan^{-1} \left(\frac{\tau \sin \phi}{1 - \tau \cos \phi} \right). \quad (2.15)$$

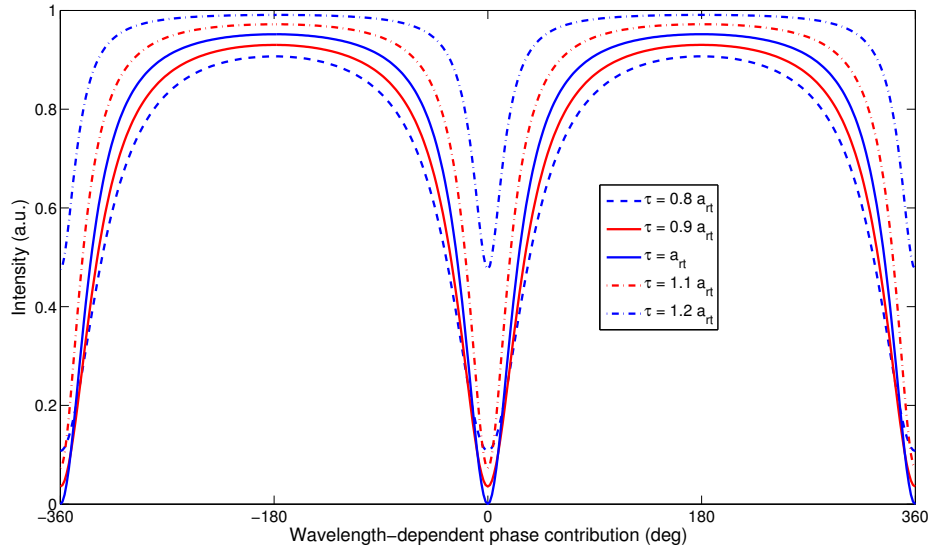


Figure 2.4: The intensity at the through port with a fixed round-trip amplitude a_{rt} and different transmission strength τ . a_{rt} used here is 0.8.

The slope of the phase shift, as shown in Fig. 2.3, becomes sharp near the resonance, so the phase shift is very sensitive to the wavelength-dependent phase contribution in the microring resonator. This enhanced phase shift can be useful in Mach-Zehnder-interferometer (MZI) devices [41].

The critically-coupled condition of the all-pass configuration occurs when transmission strength τ is equal to round-trip amplitude a_{rt} , and the transmitted field drops to 0 at resonant wavelengths. The microring resonator behaves as a notch filter, completely removing the intensity of resonant wavelengths in the spectrum. Fig. 2.4 illustrates the spectrum of various transmission strengths.

2.4 Add-Drop Configuration

Fig. 2.5 shows a microring resonator in add-drop configuration, in which 2 straight bus waveguides are placed beside the microring. Compared to all-pass configuration, the round-trip loss of the microring resonator here takes the power coupled to the other bus waveguide in account. Thus, technically, the round-trip amplitude in add-drop configuration is equivalent to the product of the round-trip amplitude and transmission strength. At steady state, the transfer functions at the through port T_{ad} and the drop port R_{ad} are given by

$$T_{ad} \equiv \frac{E_t}{E_i} = \frac{\tau_1 - \tau_2 a_r e^{-j\phi}}{1 - \tau_1 \tau_2 a_r e^{-j\phi}} \quad (2.16)$$

$$R_{ad} \equiv \frac{E_d}{E_i} = \frac{-\kappa_1 \kappa_2 a_r^{1/2} e^{-j\phi/2}}{1 - \tau_1 \tau_2 a_r e^{-j\phi}}, \quad (2.17)$$

where E_i is the field at the input, E_t is the field at the through port, E_d is the field at the drop port, τ_1 and κ_1 are transmission and coupling strength between the input bus waveguide and the microring resonator and τ_2 and κ_2 are transmission and coupling strength between the other bus waveguide and the microring resonator. Fig. 2.6 shows the intensity at the through port and the drop port, given the device is symmetric, that is, the coupling strengths at both sides are equal and there is no input signal from the add port. The critically-coupled condition is not feasible unless the microring is lossless.

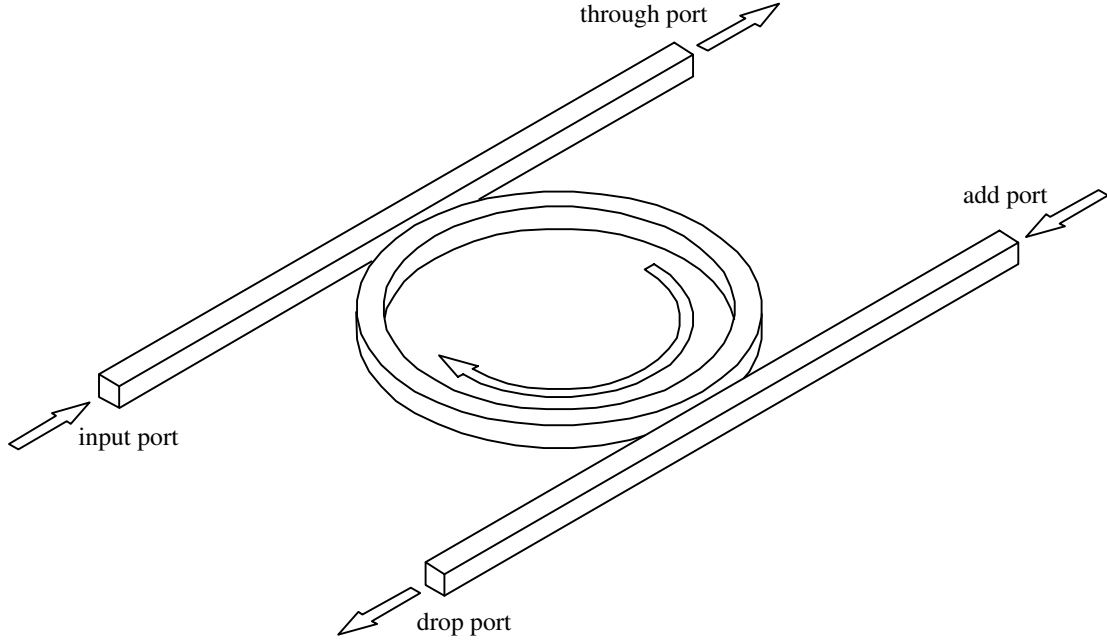


Figure 2.5: Schematic diagram of a microring resonator in add-drop configuration.

2.5 Characteristics of Microring Resonators

2.5.1 Field Enhancement

The field enhancement factor (FE) is defined as the magnitude ratio of the circulating field to the input field at resonance. For all-pass configuration, the FE can be obtained by solving Eqs (2.12) and (2.13)

$$FE_{ap} \equiv \left. \frac{E_{o1}}{E_{I2}} \right|_{\phi=0} = \left. \frac{-j\kappa}{1 - \alpha_{rt} e^{-j\phi}} \right|_{\phi=0} = \frac{\kappa}{1 - \alpha_{rt}}. \quad (2.18)$$

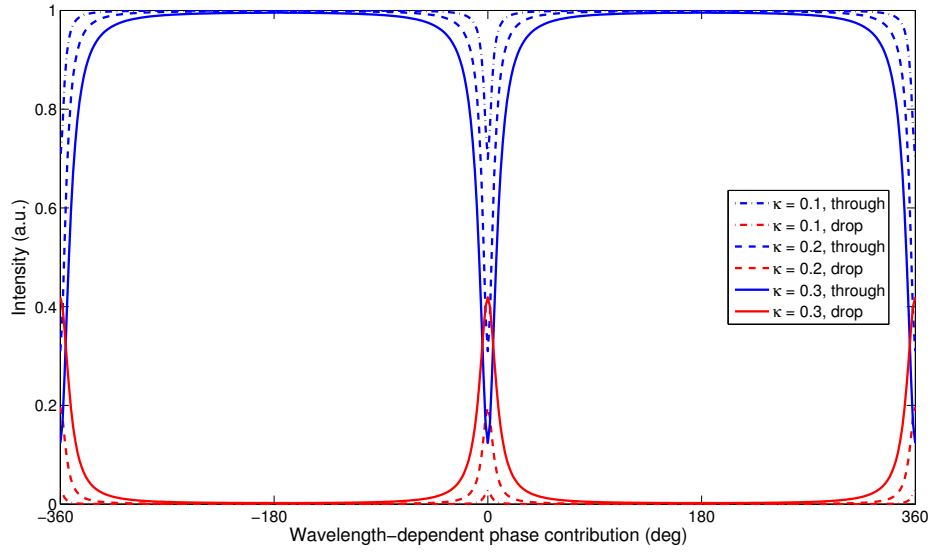
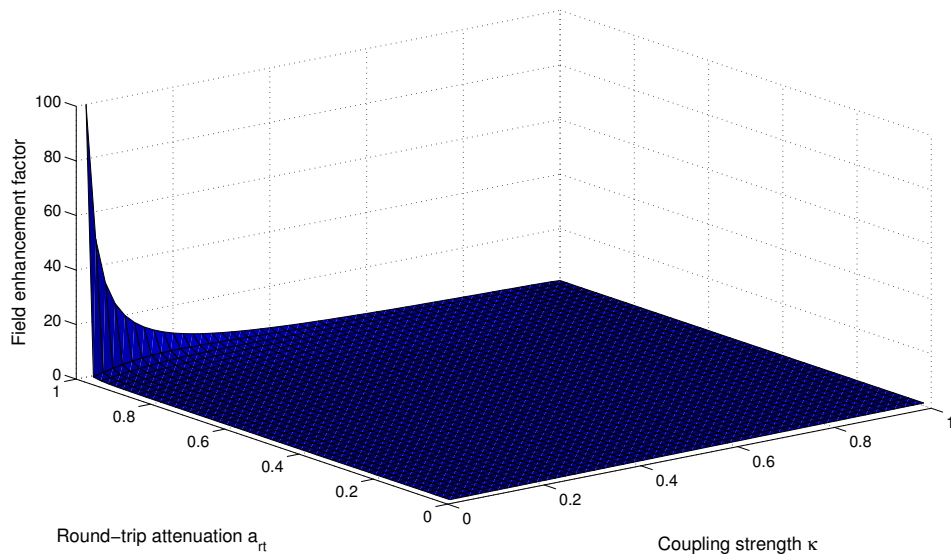


Figure 2.6: The intensity at the through port and the drop port with a fixed round-trip amplitude a_{rt} and different coupling strength τ . a_{rt} used here is 0.95.

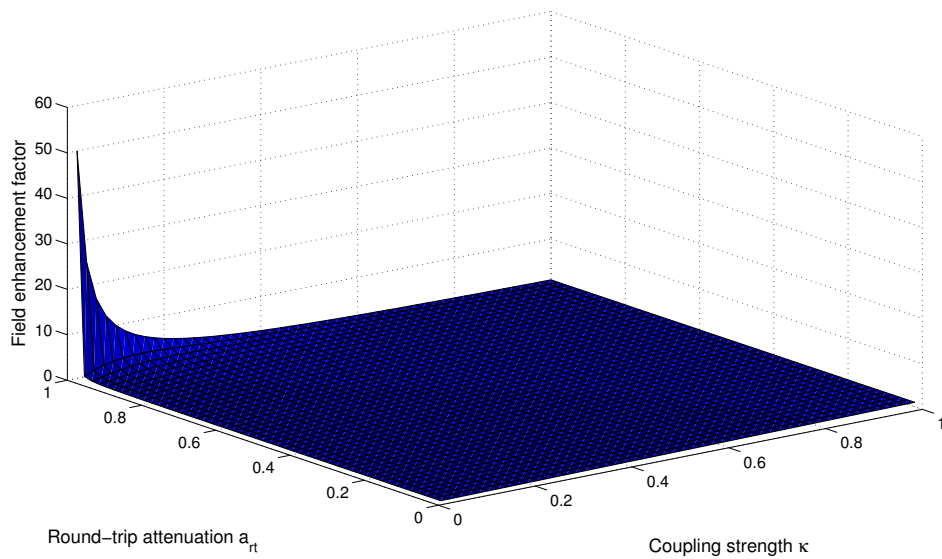
Similarly, the FE of add-drop configuration is given as

$$FE_{ad} = \left| \frac{-j\kappa}{1 - \tau^2 a_{rt} e^{-j\phi}} \right|_{\phi=0} = \frac{\kappa}{1 - \tau^2 a_{rt}}. \quad (2.19)$$

Fig. 2.7 suggests that the lower the round-trip loss, the higher the field enhancement and the higher power would be built up inside the resonator.



(a)



(b)

Figure 2.7: The field enhancement of a microring resonator (a) in all-pass configuration; (b) in add-drop configuration.

2.5.2 Free Spectral Range

The free spectral range (FSR) $\Delta\lambda$ refers to the wavelength span between two consecutive resonances. From Eq. (2.1)

$$Ln_{eff} = m\lambda_m = (m-1)\lambda_{m-1} = (m-1)(\lambda_m + \Delta\lambda). \quad (2.20)$$

Assuming the longitudinal mode number m is large, $\Delta\lambda$ is given as

$$\Delta\lambda \approx \frac{\lambda^2}{n_{eff}L}. \quad (2.21)$$

Therefore, a compact microring implies a large FSR.

2.5.3 Bandwidth

The bandwidth of a microring resonator is defined as the full width at half maximum (FWHM) of the intensity in the microring resonator. For all-pass configuration,

$$\left| \frac{-j\kappa}{1 - \alpha_r e^{-j\delta\phi}} \right|^2 = \frac{1}{2} \left| \frac{\kappa}{1 - \alpha_r} \right|^2, \quad (2.22)$$

which leads to

$$\cos(\delta\phi) = \frac{4\tau a_{rt} - \tau^2 a_{rt}^2 - 1}{2\tau a_{rt}}. \quad (2.23)$$

Using the Taylor expansion for narrow bandwidth

$$\cos(\delta\phi) \approx 1 - \frac{1}{2}(\delta\phi)^2 = \frac{4\tau a_{rt} - \tau^2 a_{rt}^2 - 1}{2\tau a_{rt}} \quad (2.24)$$

which results in

$$\delta\phi = \frac{1 - \tau a_{rt}}{(\tau a_{rt})^{1/2}}. \quad (2.25)$$

From Eq. (2.11)

$$|\delta\phi| = \left| \delta \left(\frac{2\pi}{\lambda} n_{eff} L \right) \right| = \left| \frac{-2\pi}{\lambda^2} n_{eff} L \delta\lambda \right| = \frac{2\pi}{\lambda^2} n_{eff} L |\delta\lambda|. \quad (2.26)$$

The bandwidth $\delta\lambda_{FWHM,ap}$ of all-pass configuration is given by

$$\delta\lambda_{FWHM,ap} = 2|\delta\lambda| = \frac{\lambda^2}{\pi n_{eff} L} \frac{1 - \tau a_{rt}}{(\tau a_{rt})^{1/2}}. \quad (2.27)$$

Similarly, the bandwidth $\delta\lambda_{FWHM,ad}$ of add-drop configuration is given by

$$\delta\lambda_{FWHM,ad} = \frac{\lambda^2}{\pi n_{eff} L} \frac{1 - \tau^2 a_{rt}}{\tau a_{rt}^{1/2}}. \quad (2.28)$$

2.5.4 Finesse

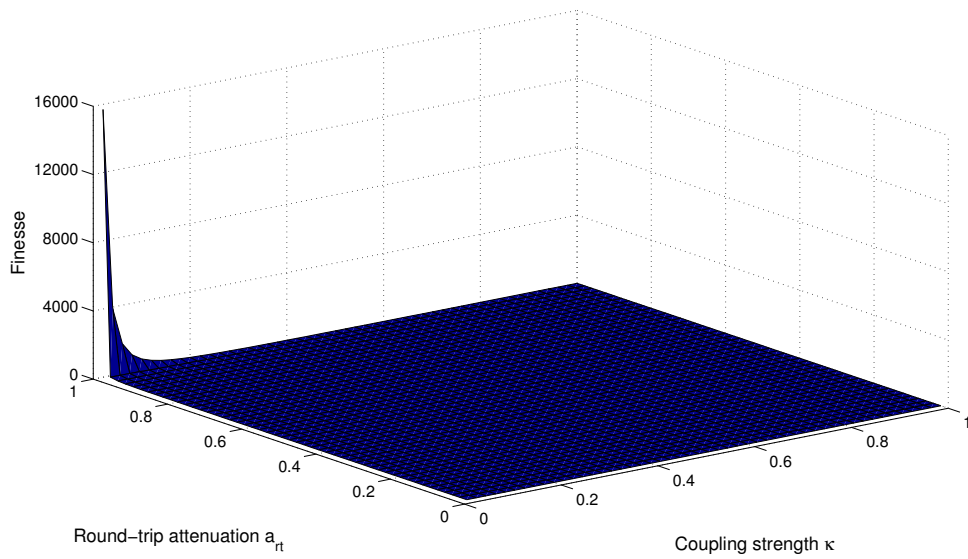
The FSR along with the bandwidth determines the number of non-overlapping channels. The finesse of a microring resonator, which presents this capability, is defined as the ratio of the FSR to the bandwidth

$$F_{ap} \equiv \frac{FSR}{\delta\lambda_{FWHM,ap}} = \frac{\pi(\tau a_{rt})^{1/2}}{1 - \tau a_{rt}}, \quad (2.29)$$

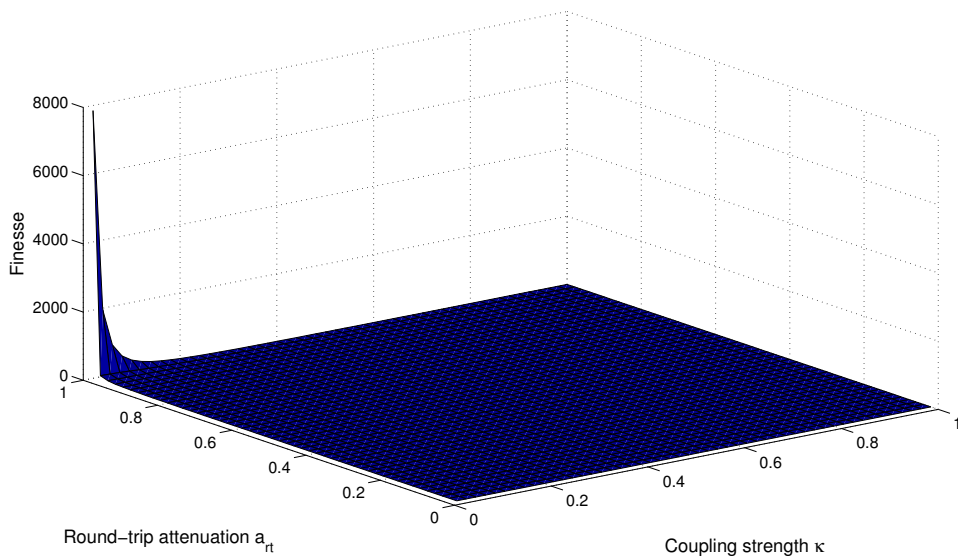
for all-pass configuration. And for add-drop configuration

$$F_{ad} \equiv \frac{FSR}{\delta\lambda_{FWHM,ad}} = \frac{\pi\tau a_{rt}^{1/2}}{1 - \tau^2 a_{rt}}. \quad (2.30)$$

Assuming the round-trip loss and the coupling strength of a microring resonator are geometric-dimension-independent, the finesse is also independent of the dimension of a microring resonator. Fig. 2.8 suggests that the lower the round-trip loss, the higher the finesse and the more channels can be carried in a microring resonator.



(a)



(b)

Figure 2.8: The finesse of a microring resonator (a) in all-pass configuration; (b) in add-drop configuration.

2.5.5 Cavity Lifetime

The cavity lifetime refers to the average time a photon stays in a microring cavity before being absorbed or coupled out. For all-pass configuration, the cavity lifetime is given by

$$\tau_{ph,ap} \equiv \frac{1}{|\delta f_{FWHM,ap}|} = \frac{\lambda^2}{c} \frac{1}{|\delta \lambda_{FWHM,ap}|} = \frac{\pi n_{eff} L (\tau a_{rt})^{1/2}}{c} = \frac{n_{eff} L}{c} F_{ap} \quad (2.31)$$

where c is the speed of light in vacuum. For add-drop configuration

$$\tau_{ph,ad} \equiv \frac{1}{|\delta f_{FWHM,ad}|} = \frac{\lambda^2}{c} \frac{1}{|\delta \lambda_{FWHM,ad}|} = \frac{\pi n_{eff} L}{c} \frac{\tau a_{rt}^{1/2}}{1 - \tau^2 a_{rt}} = \frac{n_{eff} L}{c} F_{ad} \cdot \quad (2.32)$$

Eqn. (2.30) and (2.31) imply that the number of round-trips that a photon circulating in the microring resonator before being absorbed or coupled out is equal to the finesse. In addition, the cavity lifetime serves as a limit of all-optical signal processing speed.

2.5.6 Quality Factor

The quality factor of a microring resonator Q , defined as the ratio of the stored energy to the energy lost per oscillation, indicates the ability of a resonator to store energy. Alternatively, it can be written as [7]

$$Q_{ap} \equiv \frac{\lambda}{\delta\lambda_{FWHM,ap}} = \frac{\pi n_{eff} L (\tau a_{rt})^{1/2}}{\lambda (1 - \tau a_{rt})} = \frac{n_{eff} L}{\lambda} F_{ap} \quad (2.33)$$

for all-pass configuration. Similarly, for add-drop configuration

$$Q_{ad} \equiv \frac{\lambda}{\delta\lambda_{FWHM,ad}} = \frac{\pi n_{eff} L \tau a_{rt}^{1/2}}{\lambda (1 - \tau^2 a_{rt})} = \frac{n_{eff} L}{\lambda} F_{ad}. \quad (2.34)$$

As can be seen in Eqn (2.32) and (2.33), the quality factor is dependent on the dimension of the resonator and resonance wavelength. Therefore, the finesse, instead of the quality factor, will be used to make judgment on the quality of microring resonators.

Chapter 3

Design and Fabrication of BCB Microring Resonators

3.1 Introduction

Details of the optical design of BCB microring resonators, followed by the fabrication process, are presented in this chapter. To simplify the layer structure and fabrication processing, only laterally-coupled microring resonators, in which the bus waveguides are in the same plane with the microring resonator [15], were considered in this work. The numerical simulations were done with commercial software, such as OWMS and APSS [42]–[43], programming codes.

3.2 Optical Design of BCB Waveguides and Microring Resonators

3.2.1 Layer Structure

Figure 3.1 shows the structure of a BCB channel waveguide. A substrate is needed to support BCB waveguides because they can not be free-standing. A silicon wafer, a robust and economical material, is chosen as the substrate. In addition, during the cleaving, the silicon lattice also helps to obtain devices with a smooth waveguide facet for a better coupling efficiency from fiber tips. Since the refractive index of the silicon (~ 3.5) is higher than that of the BCB (~ 1.545), the deposition of a low-index cladding layer between BCB and silicon is required to prevent

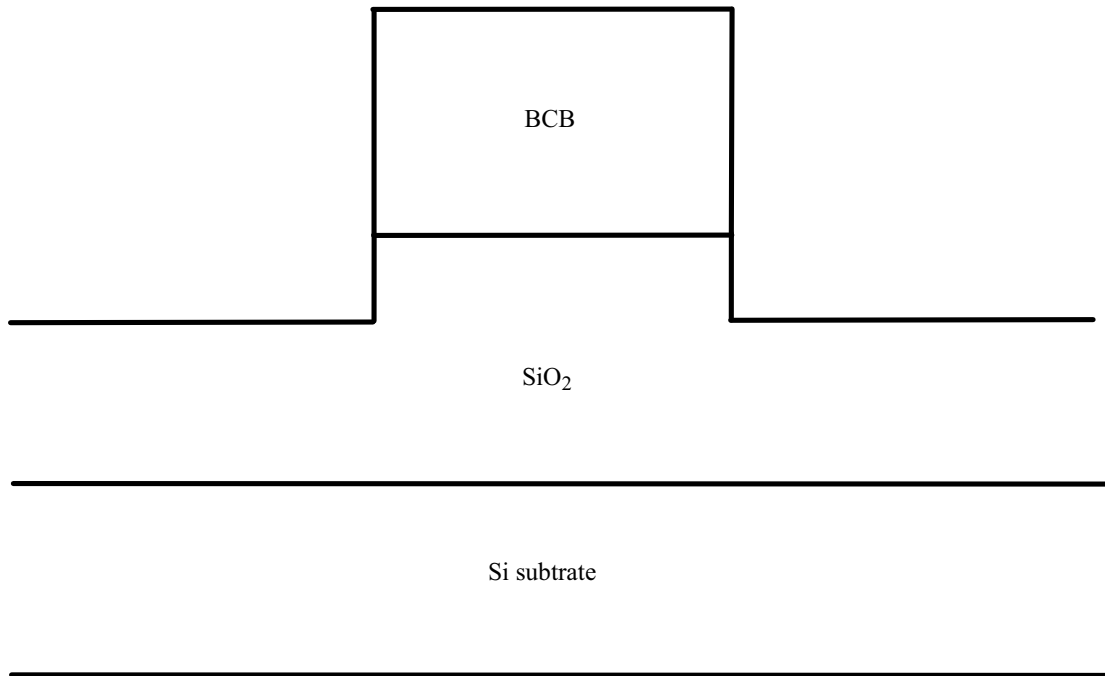


Figure 3.1: Schematic diagram of a BCB channel waveguide.

the guided wave from leaking into the silicon substrate dissipating. In this work, silicon dioxide (SiO₂) is used as the lower cladding. Moreover, the channel-waveguide scheme helps to confine the optical mode within the core.

3.2.2 Single-Mode Operation

Single-mode operation is a desirable feature in our work not merely for the compactness of the device for photonics but also for ensuring the quality of optical signal processing. Multimode waveguides, on the contrary, induce intermode coupling over propagation between the fundamental mode and higher-order even

modes - provided the waveguide is structurally symmetric and uniform and thus the overlap integral between any even mode and odd mode is 0. Subsequently, those higher-order even modes come with displeasing resonant wavelengths in the spectrum and ruin the performance of microring resonators. In addition, pulse distortion caused by modal dispersion becomes dominant at higher-order modes, which do not have a strong mode-confinement and are more susceptible to bending loss [44].

3.2.3 Coupling Constant and Coupling Strength

Consider two parallel waveguides, p and q guiding an optical mode in the z direction. Based on the coupled mode theory and perturbation analysis [39], [44], [48], the coupling constant c_{pq} can be written as

$$c_{pq}(z) = \frac{\omega \epsilon_0}{4} \iint [n_{pq}^2(x, y) - n_q^2(x, y)] E_p^*(x, y) \cdot E_q(x, y) dx dy, \quad (3.1)$$

where ω is the angular frequency of the field, ϵ_0 is the free-space dielectric constant, n_{pq} and n_q are the distribution of refractive index with both waveguides present and with only waveguide q present, and E_p and E_q are the normalized field for waveguide p and q , respectively. And the coupling strength κ is the integral over the interaction region

$$\kappa = \int c_{pq}(z) dz. \quad (3.2)$$

Compared to the ring-shaped resonant cavity, a microracetrack resonator, as shown in Fig. 3.2, extends the interaction region and effectively increases the coupling strength.

3.2.4 Propagation Loss

The impact of the propagation loss, which was alternatively termed as round-trip amplitude in chapter 2, can be large on microring devices. The propagation loss of a microring arises from the following physical effects [20], [44].

The first type of loss, the absorption loss, is material-related. The absorption loss results from molecular resonances in the material, such as electronic and vibrational transitions. These transitions cause the energy to be absorbed and stored in an excited state, but it is eventually dissipated through photon emission or lattice vibrations. Moreover, intentional dopants or unintended impurities in the material can dramatically increase its absorption loss as well [45].

The second type of loss, the bending loss, exists among bent waveguides. The evanescent field in the outer cladding has to travel faster to keep up with the optical mode. At a critical radius, the field breaks away and enters a radiating mode, resulting in energy loss in the waveguide. The bending loss can be numerically computed by conformal mapping of refractive indices in bent waveguides and by Wenzel-Kramers-Brillouin (WKB) method [46]–[47]. The bending loss can be minimized by careful waveguide design. Strong mode-confinement in the channel waveguide, as mentioned in section 3.2.3, also helps to reduce the bending loss. Fig. 3.3 shows an improved channel-waveguide scheme [26], in which the undercut pedestal increases

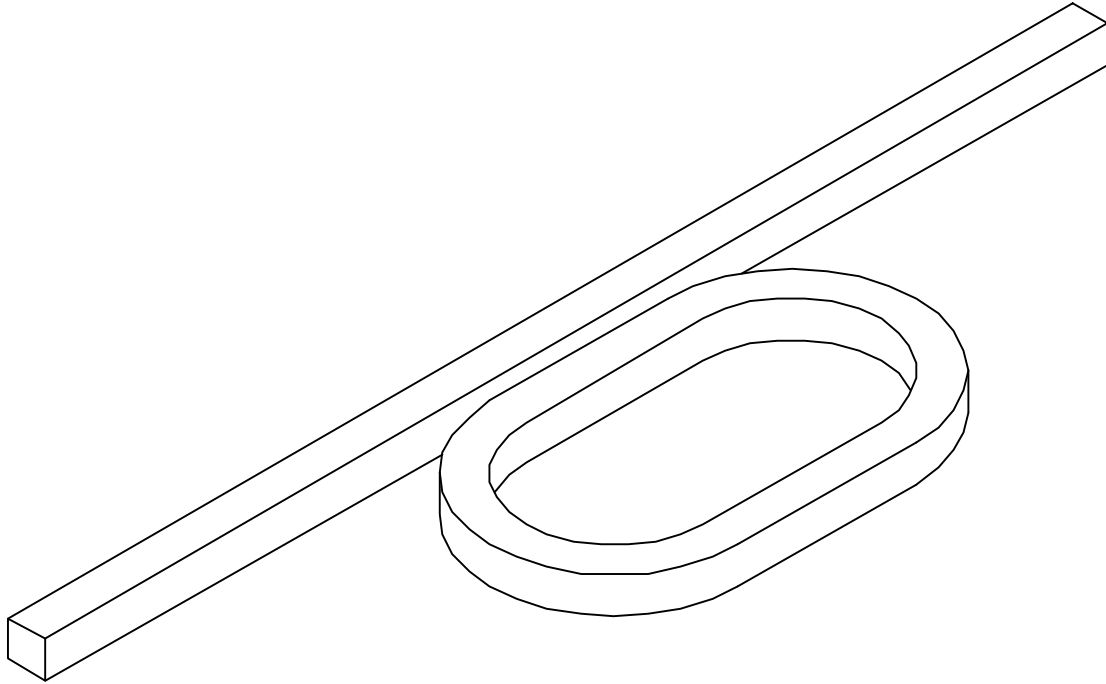


Figure 3.2: Schematic diagram of a microracetrack resonator.

the refractive-index difference between the core and lower cladding and makes the optical mode more confined in the core. The optical intensity distribution of BCB waveguides with a core of $1.8 \mu\text{m} \times 1.8 \mu\text{m}$ and a bent radius of $10 \mu\text{m}$ is shown in Fig. 3.4. The higher and the narrower pedestal of a waveguide structure, the less evanescent-field leaks into cladding. A simulation on the bending loss of a BCB microring resonator with a radius of $10 \mu\text{m}$ is shown in Fig. 3.5, suggesting compact and low-loss BCB microring devices are feasible regardless of low refractive index of BCB polymer.

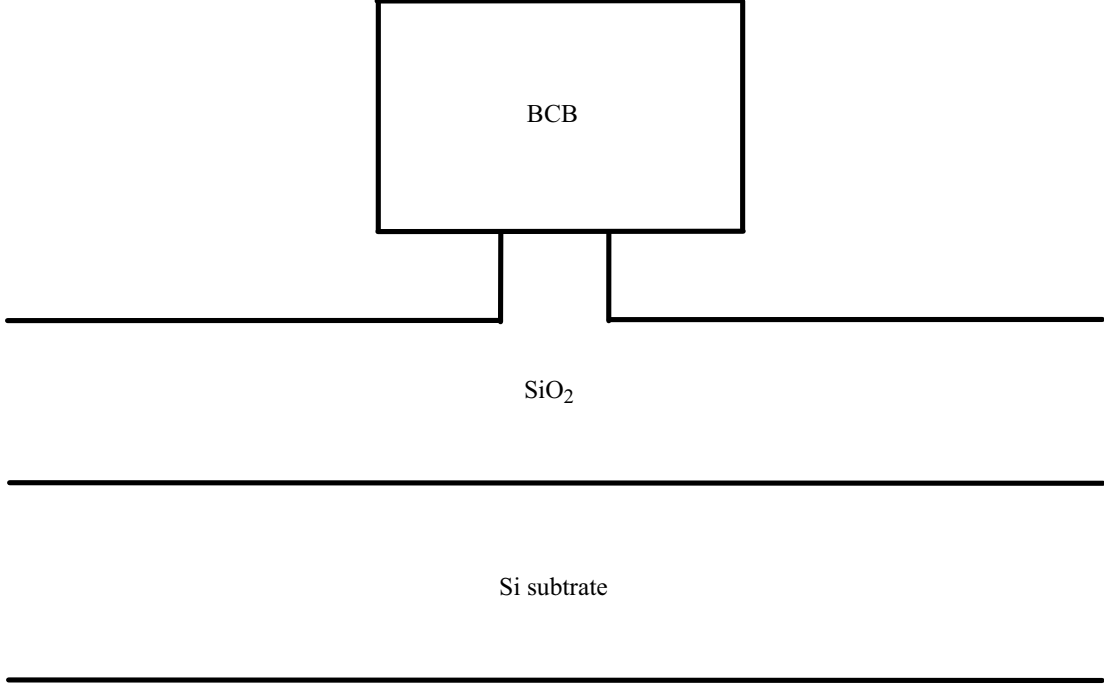
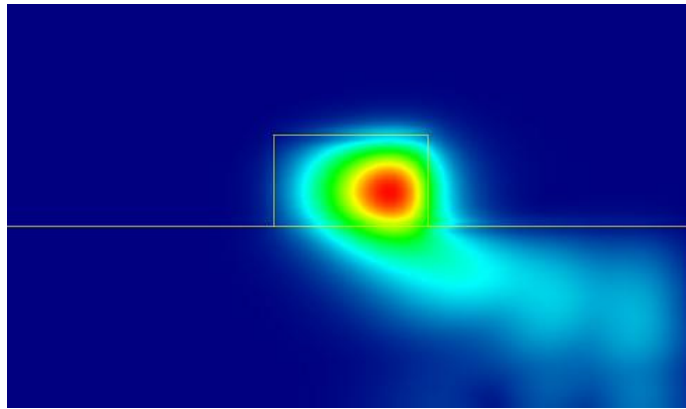


Figure 3.3: Schematic diagram of a BCB undercut channel waveguide.

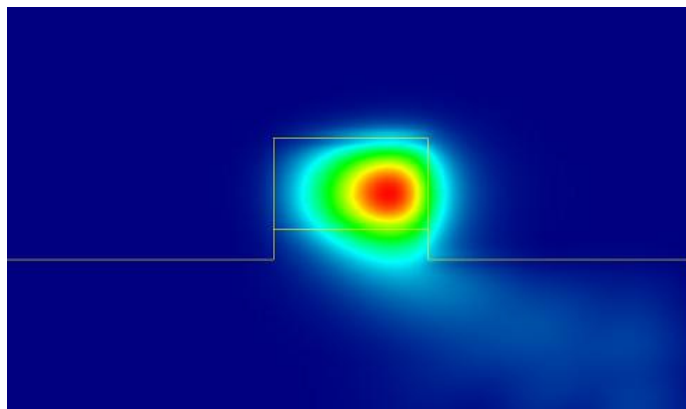
The third type of loss in a microring resonator is the scattering loss, which results from the surface roughness at waveguide sidewalls. The attenuation constant of the scattering loss α_{st} is given by [20]

$$\alpha_{st} = 2\sigma^2 (n_{eff}^2 - n_c^2) k_0^2 \frac{k_x}{\beta} E_s^2. \quad (3.1)$$

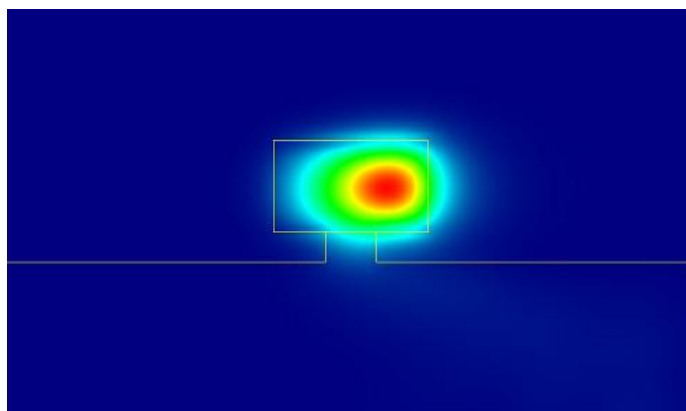
where σ is the root-mean-square (RMS) surface roughness, n_c is refractive index of the cladding, k_0 is the free-space propagation vector which is numerically equal to $2\pi/\lambda$, k_x is the transverse component of the propagation vector in the waveguide, β is



(a)



(b)



(c)

Figure 3.4: The optical intensity distribution of a bent BCB waveguide (a) in regular scheme, (b) in channel-waveguide scheme, (c) in undercut-channel-waveguide scheme.

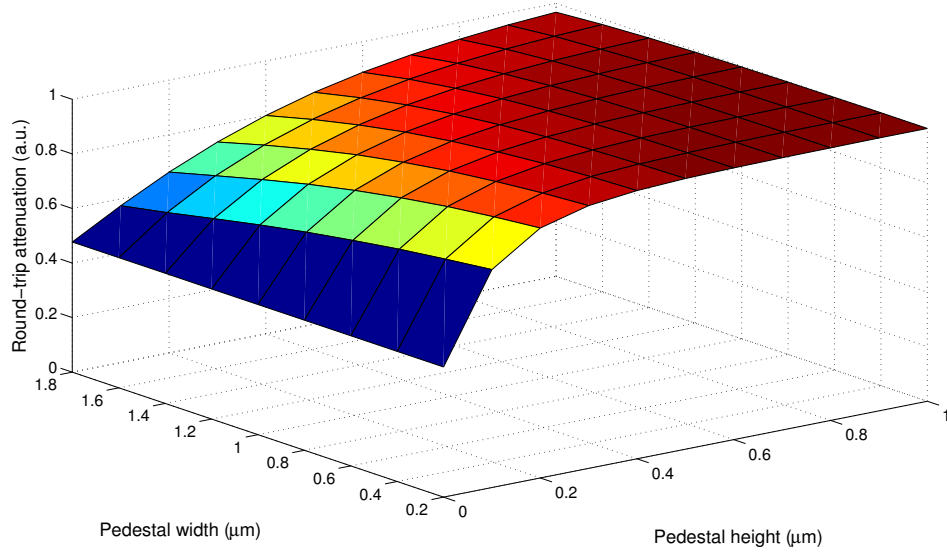


Figure 3.5: Simulated round-trip amplitude of a BCB microring resonator with a core of $1.8 \mu\text{m} \times 1.8 \mu\text{m}$ and a bent radius of $10 \mu\text{m}$.

the longitudinal component, and E_s is the normalized field at the waveguide surface.

Lastly, in microracetracks, the junction loss due to the modal mismatch appears at the junctions between straight and curved waveguide sections. Fig. 3.6 illustrates the modal mismatch with the optical intensity distribution in different sections of BCB microracetracks. The junction loss can be minimized by introducing a lateral offset at the junctions [20].

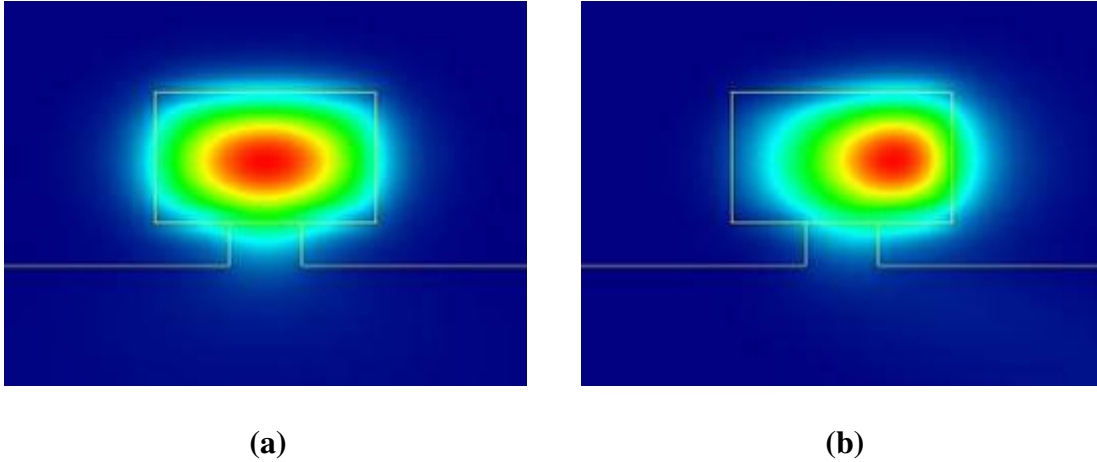


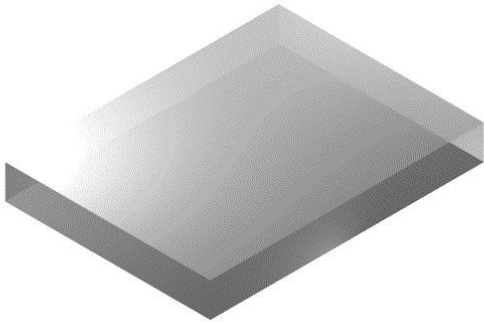
Figure 3.6: The optical intensity distribution (a) in the straight section and (b) in the curved section of a BCB microracetrack. The curved section has a radius of 10 μm .

3.3 Fabrication Steps

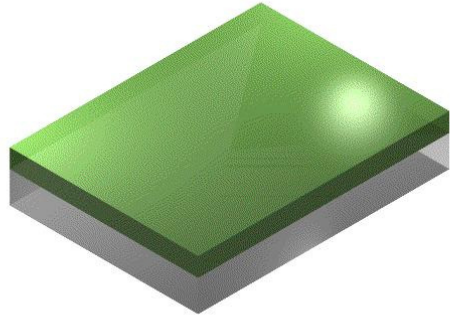
The complete process of BCB microring devices is illustrated in Fig. 3.7.

3.3.1 Sample Preparation

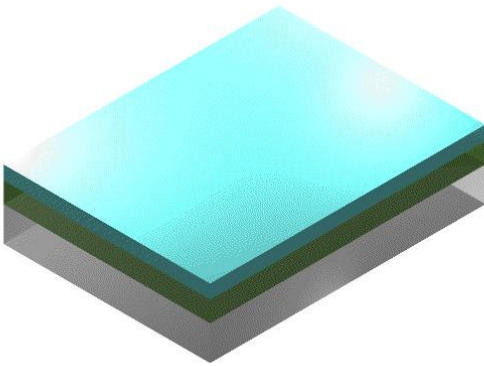
A silicon wafer is cleaved into 16 mm \times 16 mm pieces for samples, which are successively cleaned by solvent rinse in acetone, methanol and blow-dried by nitrogen (N_2).



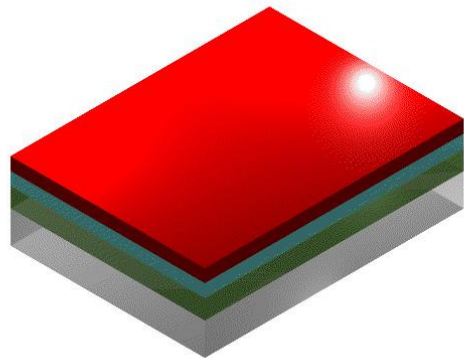
(a)



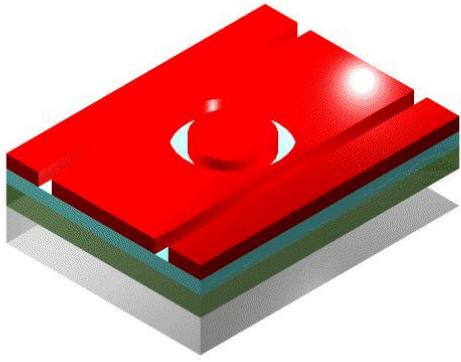
(b)



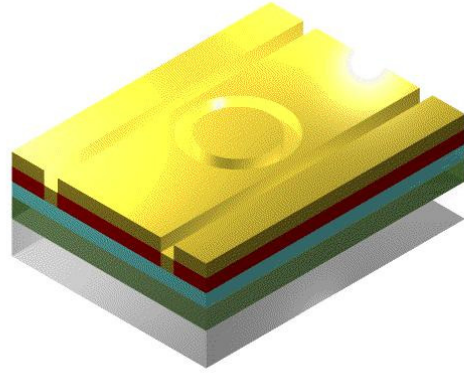
(c)



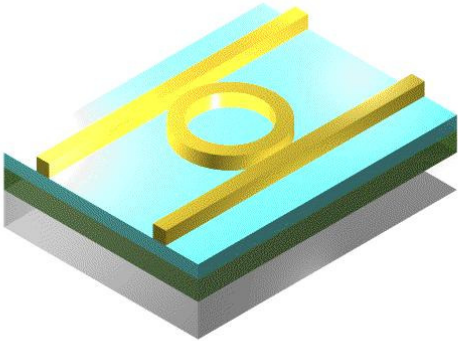
(d)



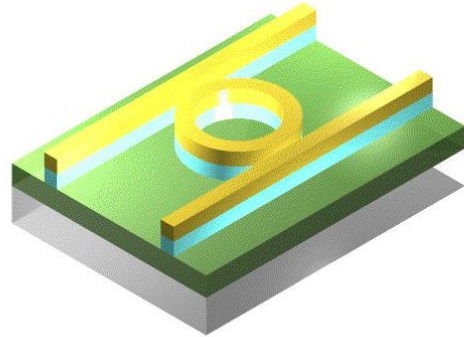
(e)



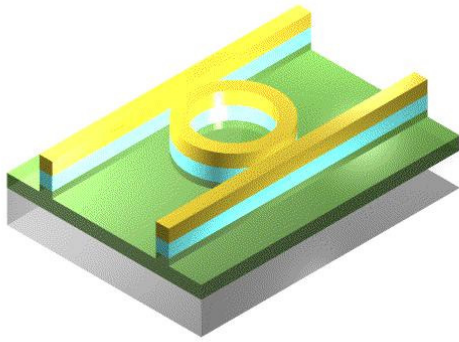
(f)



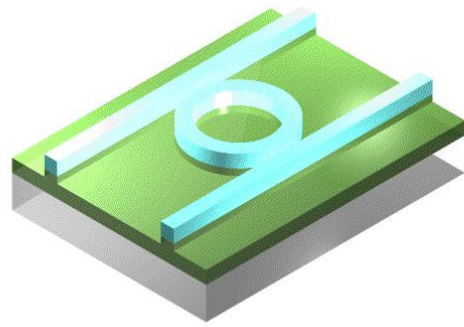
(g)



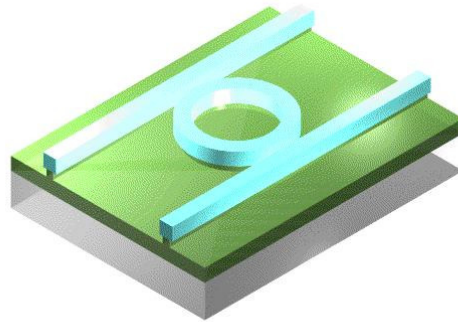
(h)



(i)



(j)



(k)

Figure 3.7: Process flow for BCB microring resonators: (a) substrate preparation, (b) SiO_2 deposition, (c) BCB deposition, (d) photoresist spin-coat, (e) photolithography, (f) aluminum deposition, (g) photoresist lift-off, (h) BCB etching, (i) SiO_2 etching, (j) aluminum removal, and (k) wet etching.

3.3.2 SiO₂ Deposition

A 5- μm layer of SiO₂ is deposited in a plasma-enhanced chemical vapor deposition (PECVD) chamber at 300 °C using silane (SiH₄) and nitrous oxide (N₂O) as reactive gases. This layer is used as lower-cladding of the waveguide structure.

3.3.3 BCB Deposition

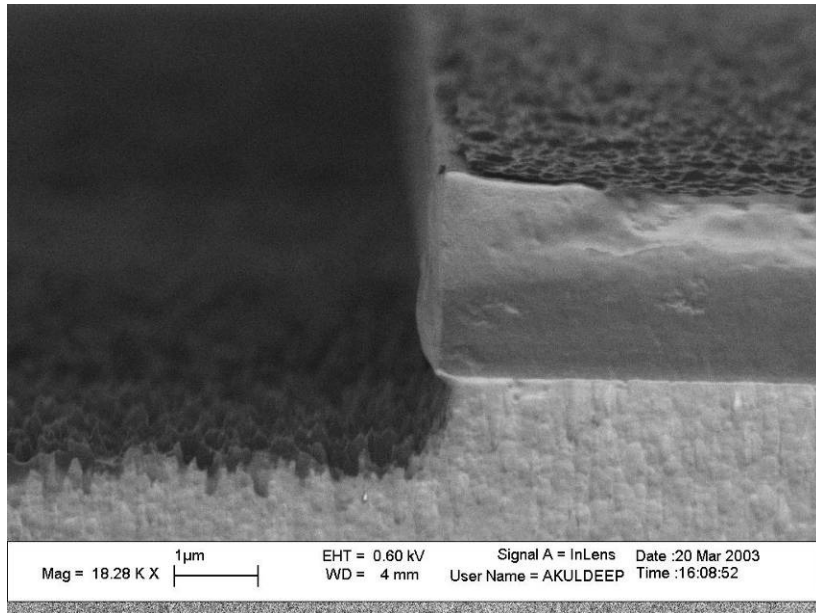
An adhesion promoter, AP3000 (Dow Chemical) is first spun on the SiO₂ film, followed by a spin-coat of a 1.8- μm -thick BCB layer using Cyclotene 3022-46 (Dow Chemical). Then, the whole sample is baked on a hotplate and thermally cured in a N₂-filled tube furnace at 250 °C.

3.3.4 Photolithography

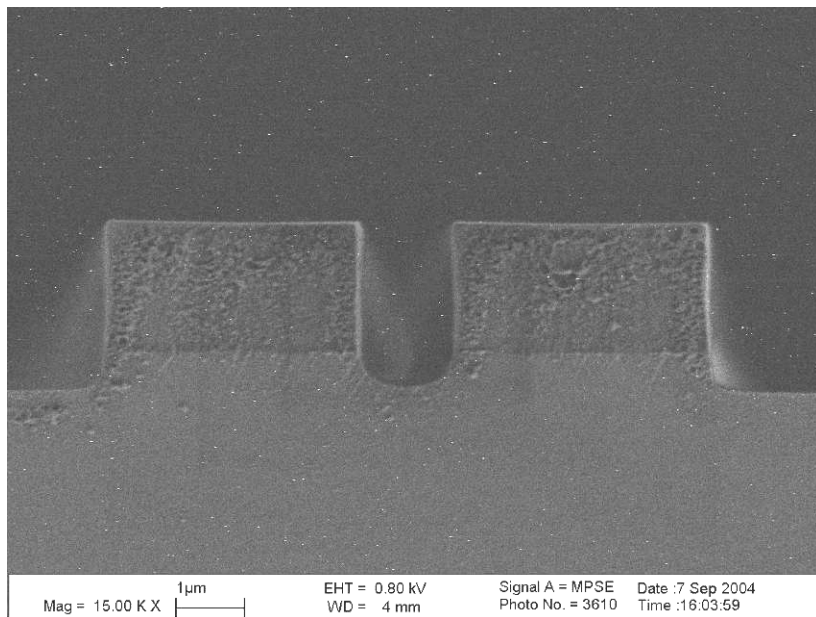
A negative photoresist, NR7-1000PY (Futurrex) is spun on the BCB film and pre-baked. The photoresist is exposed on a 5 \times projection aligner and subsequently post-baked and developed in RD6 developer (Futurrex) to form the photoresist pattern.

3.3.5 Etch-mask Deposition

A 100-nm-thick aluminum layer, which is used as an etch mask, is deposited by an electron-beam evaporator. A SiO₂ layer, which creates a bigger etching bias, was previously used as an etch mask, but its rough residue on the BCB core increased



(a)



(b)

Figure 3.8: SEM image of BCB waveguides using (a) a SiO₂ etching mask; (b) an aluminum etching mask. The residue of SiO₂ cap remained on the BCB waveguide.

the scattering loss at the waveguide surface [26]. Fig 3.8 shows scanning electron microscope (SEM) images of BCB waveguides with different etching masks.

3.3.6 Pattern Transfer

The sample is first soaked in the acetone. The photoresist pattern is transferred to the aluminum layer by lifting-off unexposed photoresist along with the aluminum on top.

3.3.7 Anisotropic Dry-Etching

The BCB core is etched in the reactive ion etching (RIE) system using sulfur hexafluoride (SF_6) and oxygen (O_2) plasma [49]. Once the BCB is etched to the core-cladding boundary, the SiO_2 cladding is etched in the RIE using trifluoromethane (CHF_3) and O_2 plasma for the channel waveguide scheme.

3.3.8 Etch-Mask Removal

The sample is soaked in a basic solvent, OPD-4262 (Olin), to remove all aluminum etch mask.

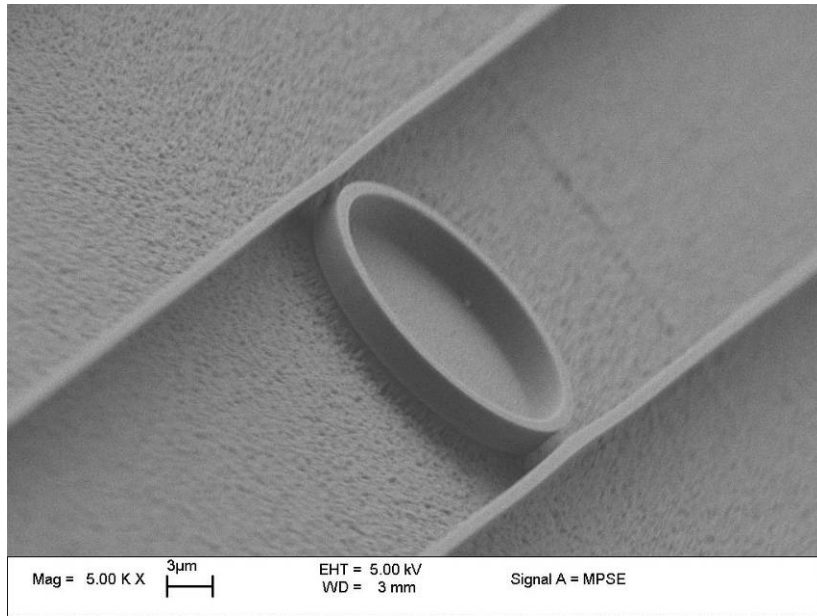
3.3.9 Sample Cleaving

A thick layer of a photoresist OiR 908-35 (Olin) is spun on the sample and baked to protect BCB devices during the cleaving. After the sample is cleaved into 3 to 4 mm pieces, the photoresist is removed by acetone.

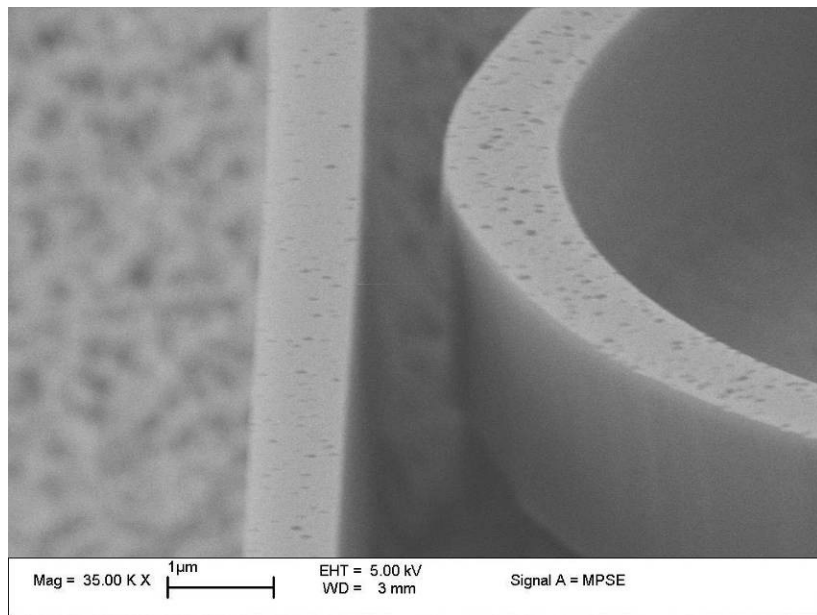
3.3.10 Isotropic Wet-Etching

The sample is soaked in buffered hydrofluoric acid (BHF), allowing the SiO₂ cladding to be isotropically etched for the undercut channel waveguide scheme.

A fabricated BCB microring resonator is shown in Fig. 3.9. It is evident that fabricating BCB microring devices with the recipe mentioned above is plausible.



(a)



(b)

Figure 3.9: (a) A SEM picture of a fabricated BCB microring resonator. (b) A clear coupling gap between the bus waveguide and the microring cavity.

Chapter 4

Single-Microring Devices

4.1 Introduction

A few BCB single microring devices are demonstrated in this chapter. The add-drop filters have a wide FSR and a high finesse. Notch filters were implemented with a negative coupling gap. The fabricated BCB microring devices are the smallest in this class of devices.

The test setup is shown in Fig. 4.1. The input beam from a tunable laser at 1550-nm window is first polarized before being sent into the device. The conically-tipped fibers are positioned by a 3-axis auto-align system at both input and output to ensure a good coupling efficiency to the facet of the device. A power meter collects data of the output beam. A computer commands the wavelength as well as the power of the tunable laser and fetches data from the power meter.

4.2 Add-Drop Filters

4.2.1 High-Extinction and High-Out-of-Band-Rejection Racetrack

Fig. 4.2 shows the measured TM-polarized spectral response at the through port and the drop port from a BCB microracetrack with a radius of 20 μm , a straight coupling section of 10 μm , and both the coupling gaps of about 0.5 μm . The waveguide had a cross section of 1.8 $\mu\text{m} \times 1.8 \mu\text{m}$. The device has a FSR of 10.7 nm,

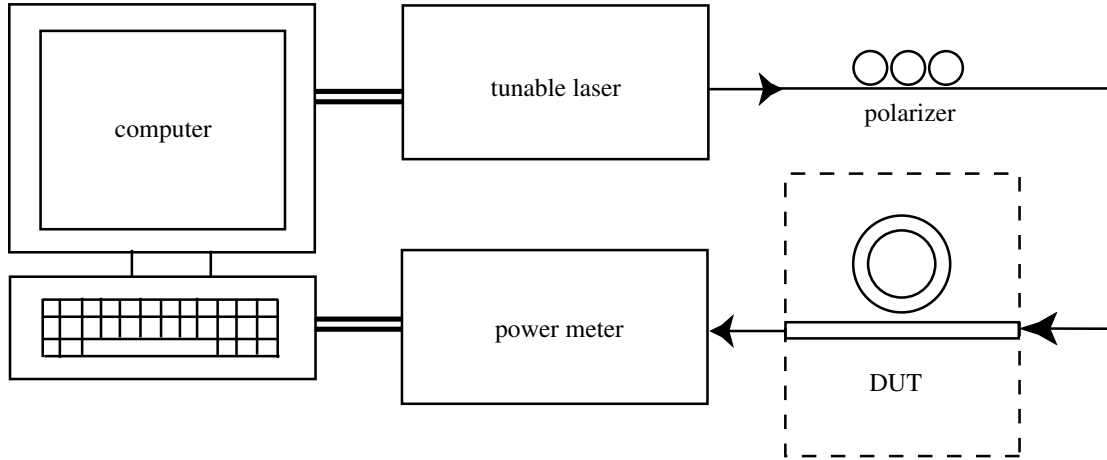
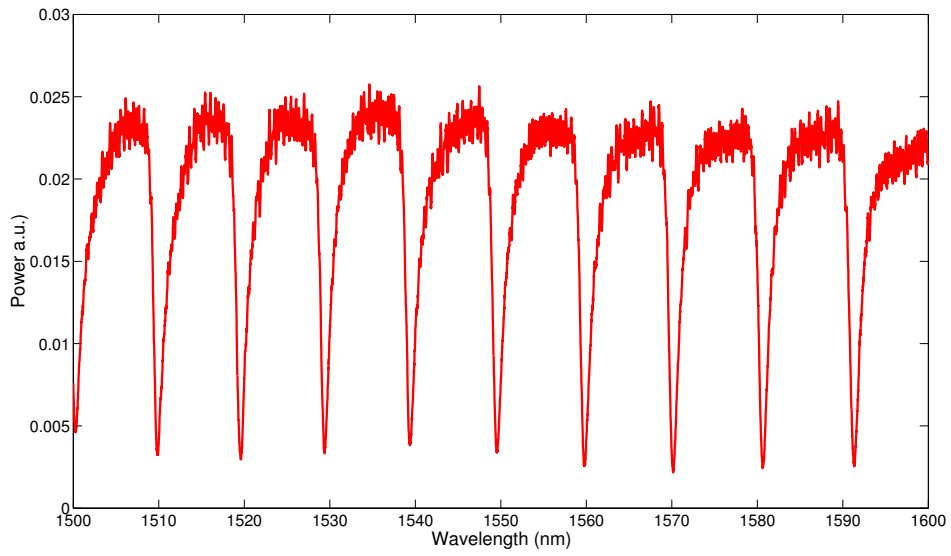
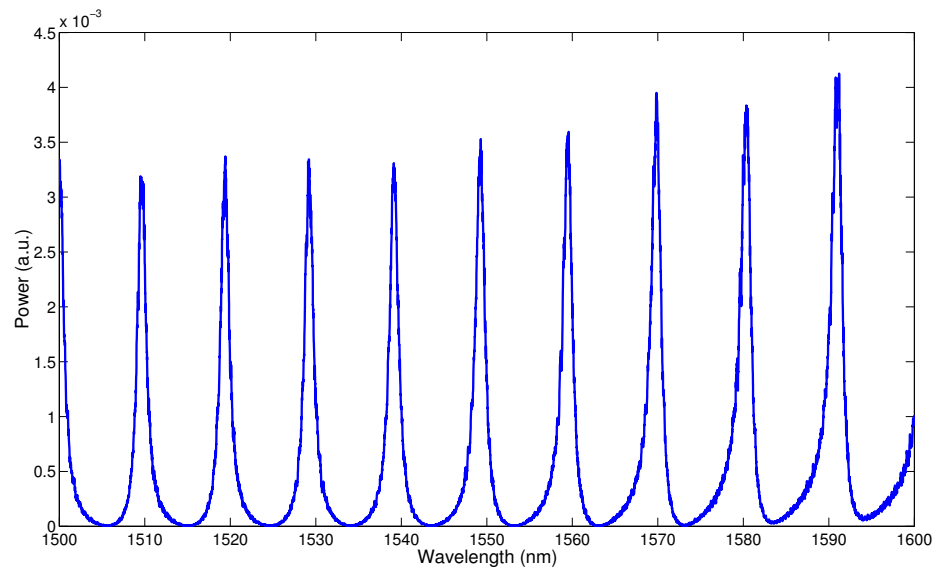


Figure 4.1: Setup for device testing.

a finesse F of 8, a maximum extinction, defined as the ratio between the off-resonance power to the on-resonance power, of 11 dB at the through port, and a maximum out-of-band rejection, defined as the ratio between the on-resonance power to the off-resonance power, of 31 dB at the drop port. Based on the measurement, the coupling strength κ is estimated as 46% and round-trip amplitude a_{rt} is about 82%. The coupling-gap width of this device was approaching the resolution limit of the ultraviolet (UV) photolithography, and it might have led to incomplete etching inside the gap and a rougher waveguide sidewall, increasing the scattering loss in the resonator.



(a)



(b)

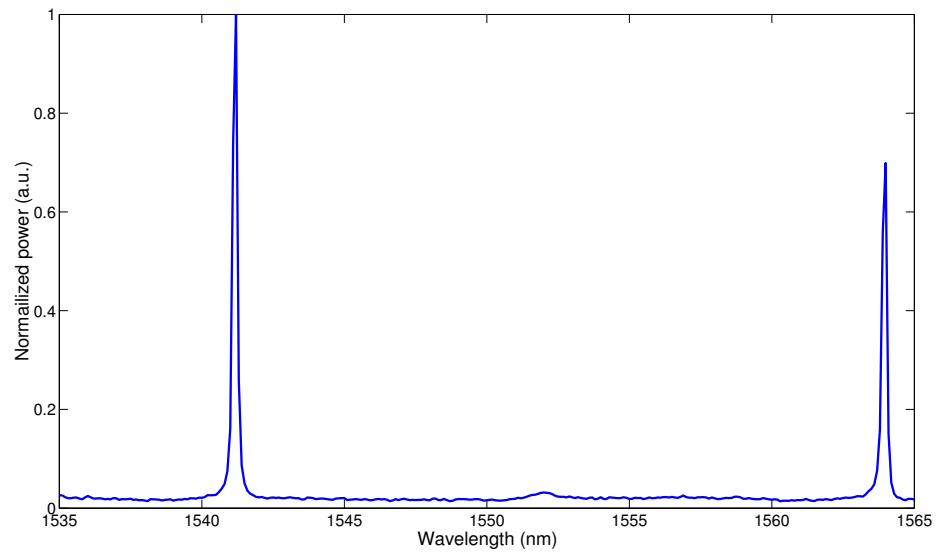
Figure 4.2: Measured spectral response of a BCB microracetrack at (a) the through port and (b) the drop port. The racetrack has a radius of $20\ \mu\text{m}$ and a straight coupling section of $10\ \mu\text{m}$.

4.2.2 Compact, Wide-FSR, and High-Finesse Microrings

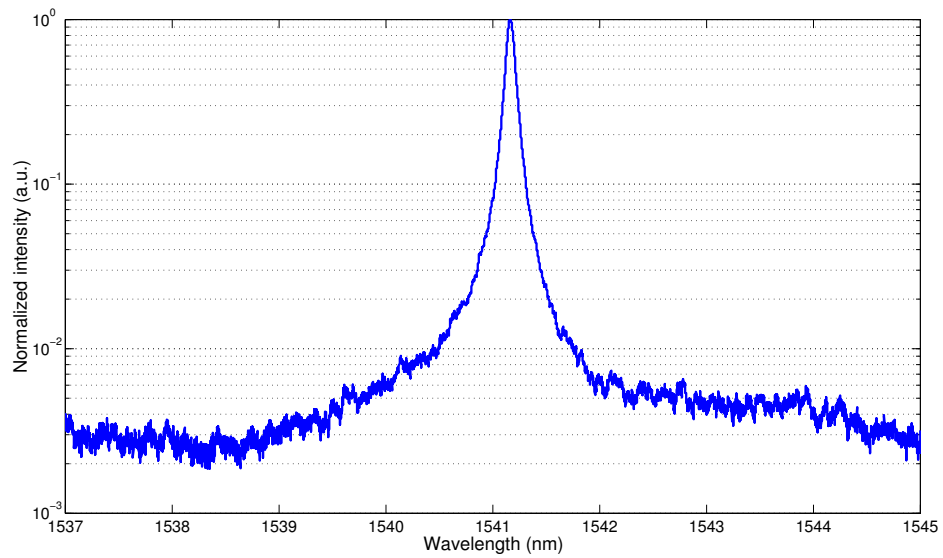
As discussed earlier in chapter 2, the loss-dependent finesse determines the capacity of a microring. Therefore, it is necessary to reduce the round-trip loss for high finesse microrings. Microrings, instead of microracetracks, with slightly wider coupling gaps were fabricated for this purpose.

Fig. 4.3 shows the measured TM-polarized spectral response at the drop port from a BCB microring with a radius of 10 μm and coupling gaps of 0.65 μm . The device has a FSR of 24.1 nm, a finesse F of 285, a quality factor Q of 20000, and a maximum out-of-band rejection of 29 dB. Based on the measurement, the coupling strength κ is estimated as 6%, round-trip amplitude a_{rt} is about 99%, and the field enhancement factor FE is about 5.7. The scattering loss at sidewall surface, although small, is responsible for the loss of the microring.

Furthermore, given the extremely low round-trip loss of the 10- μm -radius device, an ultra-compact microring with a radius of only 5 μm , arguably the smallest polymer microring in terms of the microring circumference, was fabricated and tested. Fig. 4.4 shows the optical micrograph of the device and its measured drop-port spectrum of the microring with coupling gaps of 0.7 μm . The device has a FSR of 43 nm, a finesse F of 132, and a maximum out-of-band rejection of 26 dB. The estimated κ is 3%, round-trip amplitude a_{rt} is about 98%, and the field enhancement factor FE is about 1.4. Like the 10- μm -radius microring mentioned above, the scattering loss is responsible for the loss of this 5- μm -radius resonator.

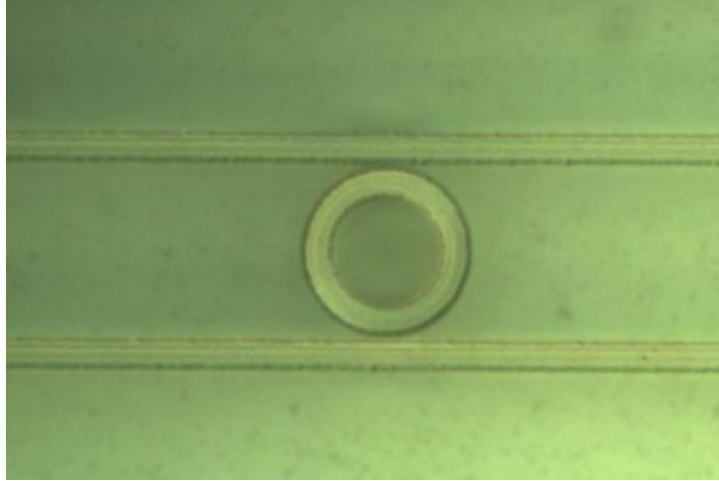


(a)

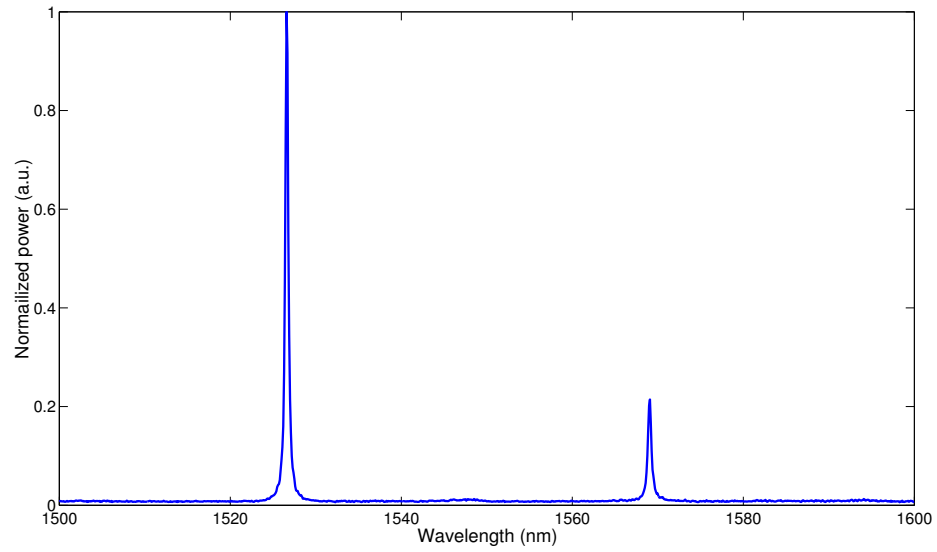


(b)

Figure 4.3: (a) Drop-port response of a BCB microring with a radius of 10 μm and (b) a detail scan at the resonance wavelength in logarithm scale.



(a)



(b)

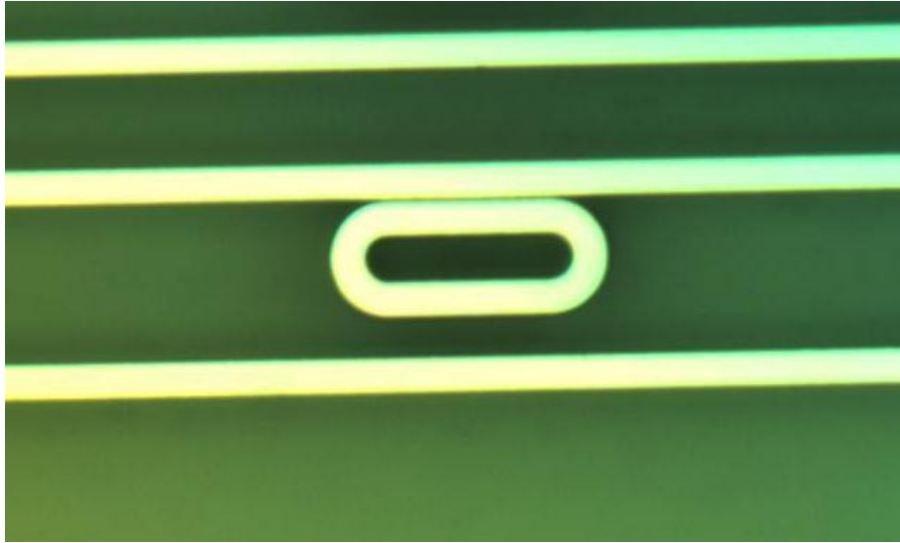
Figure 4.4: (a) Optical micrograph of a BCB microring resonator with a radius of 5 μm . (b) Drop-port spectrum of the BCB device.

4.3 Notch Filters

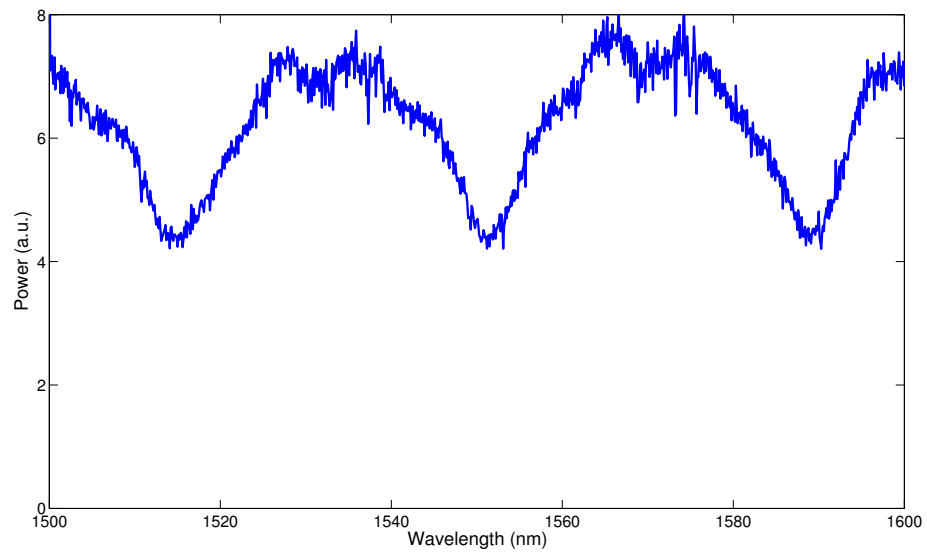
4.3.1 Ultra-Compact Microring Notch Filter

Fig. 4.5 shows the measured transmission spectrum of a BCB racetrack. The racetrack has a radius of only 2.5 μm , arguably the smallest curvature in all polymer microring devices ever made, a straight section of 10 μm , and a coupling gap of 0.5 μm . The device has a FSR of 38 nm and an extinction of 4 dB. Based on the measurement, the coupling strength κ is estimated as 58% and the round-trip amplitude a_{rt} is about only 30%. The junction loss at straight and curved section as well as the bending loss dominantly increases the loss of the resonator.

The mismatch between the loss and the coupling, or the attenuation and the transmission, results in a shallow extinction at the resonance wavelength for this under-coupled microring resonator. Reducing the narrow coupling gap increases the coupling efficiency, but also the loss because of the high scattering loss caused by the limitation of photolithography resolution on coupling gap and the following etching inside the gap. For microrings with a wider coupling gap, the mismatch is even larger, so the extinction is too shallow to be noticed in the spectrum affected by the Fabry-Perot resonance of the bus waveguide.



(a)



(b)

Figure 4.5: (a) Optical micrograph of a BCB microracetrack resonator with a radius of $2.5 \mu\text{m}$ and a straight coupling section of $10 \mu\text{m}$. (b) Measured transmission spectrum of the BCB device.

4.3.2 Negative-Gap Microring Notch Filters

Limited by the resolution of UV photolithography, the width of the coupling-gap was no less than $0.5\ \mu\text{m}$ and thus imposed a constraint on the achieved coupling strength. Although smaller gaps can be patterned with electron-beam lithography or nanoimprint technique [19], [28], etching bias for deep gaps makes the actual gap width inconsistent from time to time, even while the waveguides are fused. Alternatively, the vertically coupling scheme requires no coupling gaps, and the coupling strength can be precisely controlled by the thickness of buffer layer between microrings and bus waveguide [38]. However, the whole fabrication procedure is complicated and sometimes mistake-prone.

Another novel approach to increase the coupling strength is the negative-gap-coupling scheme. Unlike microrings with clearly etched gaps, the negative-gap microring is overlapped and merged with the bus waveguide, as illustrated in Fig. 4.6. Coupling sections in negative-gap coupling scheme essentially behave as multimode interference (MMI) couplers [50]. Here, the negative-gap coupling requires shorter interaction region and reduces the size of the devices. In Fig. 4.7, a simulation based on finite-difference time-domain method (FDTD) shows trends of the coupling and the loss for a BCB microring with a radius of $15\ \mu\text{m}$ [51]. In addition, the coupling strength by negative-gap coupling is larger than the one by “positive-gap” coupling.

Fig. 4.8 shows the measured transmission spectrum of negative-gap BCB devices. The microring has a radius of $15\ \mu\text{m}$ and a coupling gap of $-0.6\ \mu\text{m}$. The device has a FSR of $16.1\ \text{nm}$ and a maximum extinction of $29\ \text{dB}$. The estimated κ is

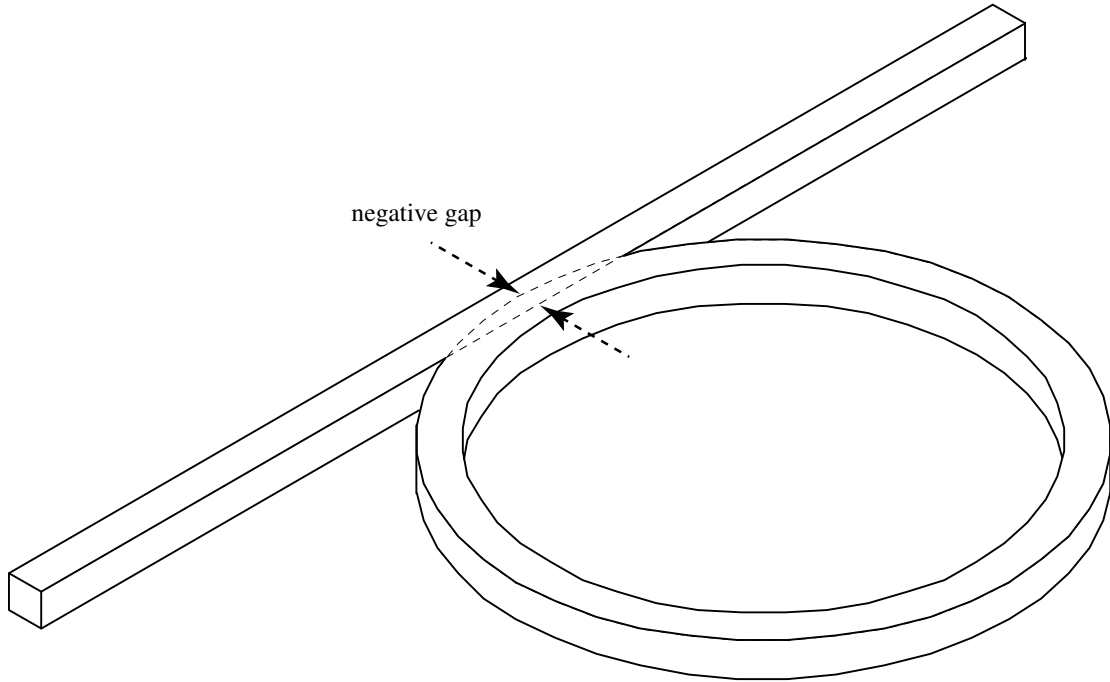


Figure 4.6: Schematic diagram of a negative-gap microring resonator.

64% and a_{rt} is 75%, showing that the microring is critically coupled. Shown in Fig. 4.9 is the measured transmission spectrum of negative-gap BCB devices. The microring has a radius of 15 μm , a straight coupling section of a 20 μm , and a coupling gap of -0.2 μm . The device has a FSR of 11.2 nm and a maximum extinction of 24 dB.

It is much easier to design critically coupled microring resonators with negative coupling gaps to achieve notch filters with very high extinction. However, compared with positive-gap microrings, the round-trip loss for negative-gap microrings is also large. The extra loss results from the modal mismatch between the ring waveguide and the merged coupling area.

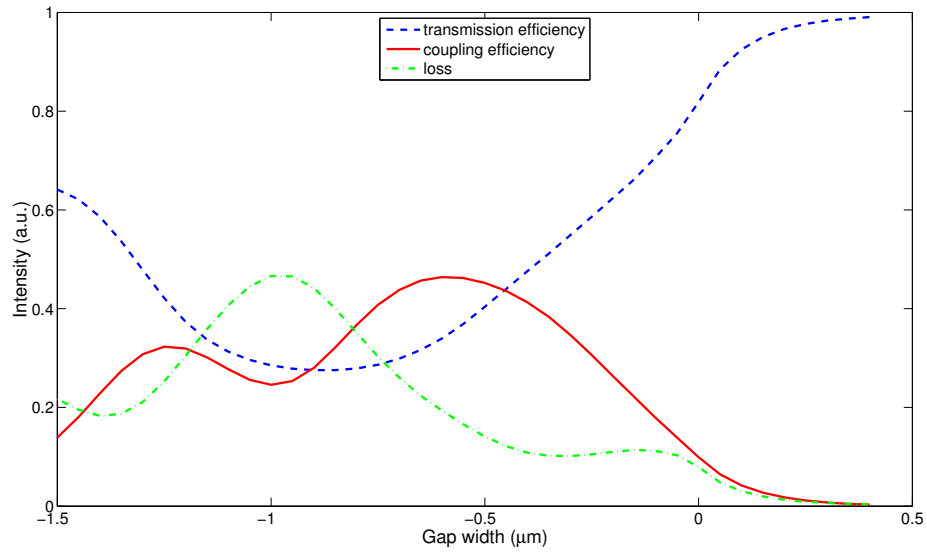
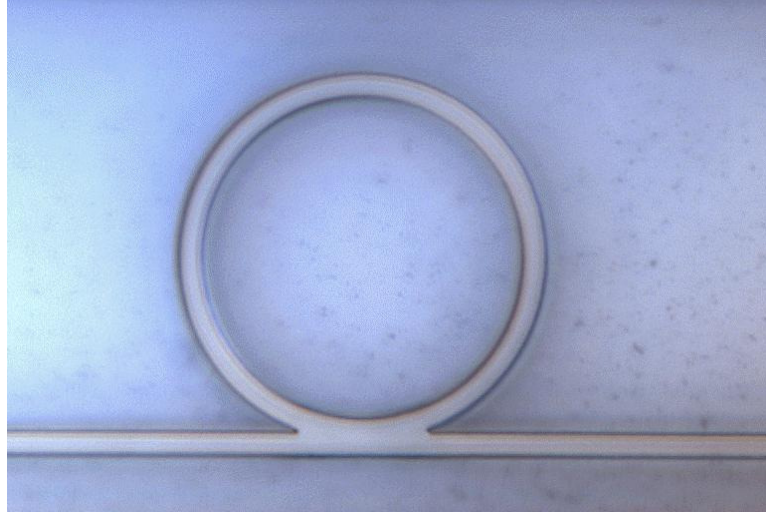
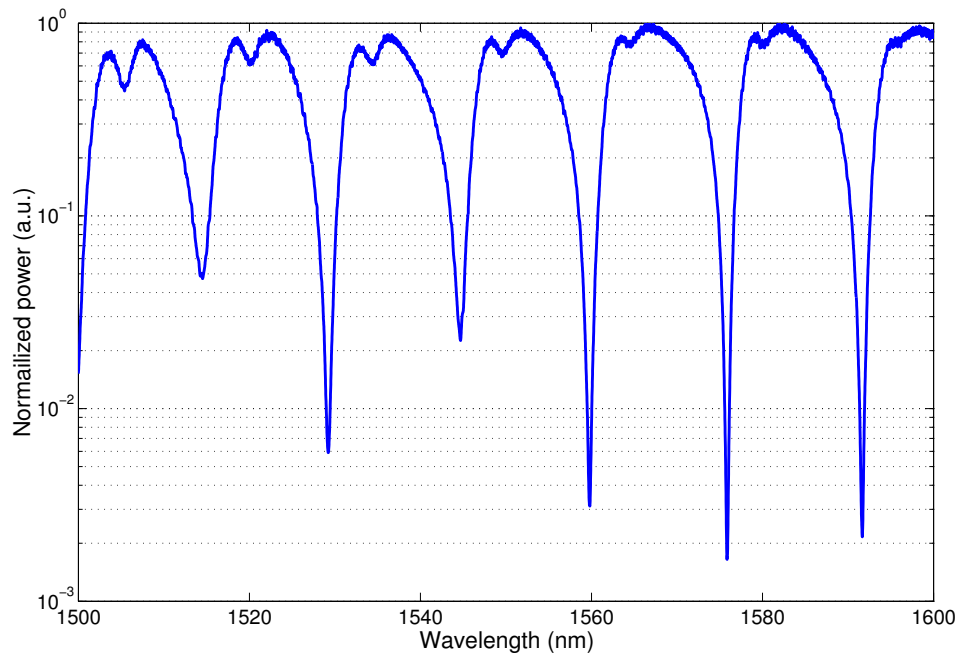


Figure 4.7: A FDTD simulation on transmission response at 1550 nm of a BCB microring device with a radius of 15 μm .

It is not suitable to apply the negative-gap-coupling scheme to the add-drop configuration, because the out-of-band rejection of the add-drop filter is low given the same coupling efficiency and round-trip loss as the all-pass configuration. In addition, the modal coupling from the higher modes in merged area might cause the resonator to be in multimode operation, in which unexpected signals would interfere with the device performance.

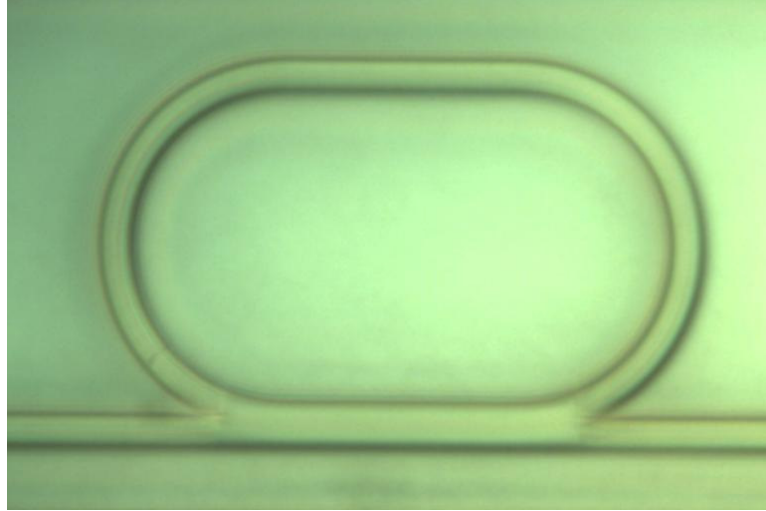


(a)

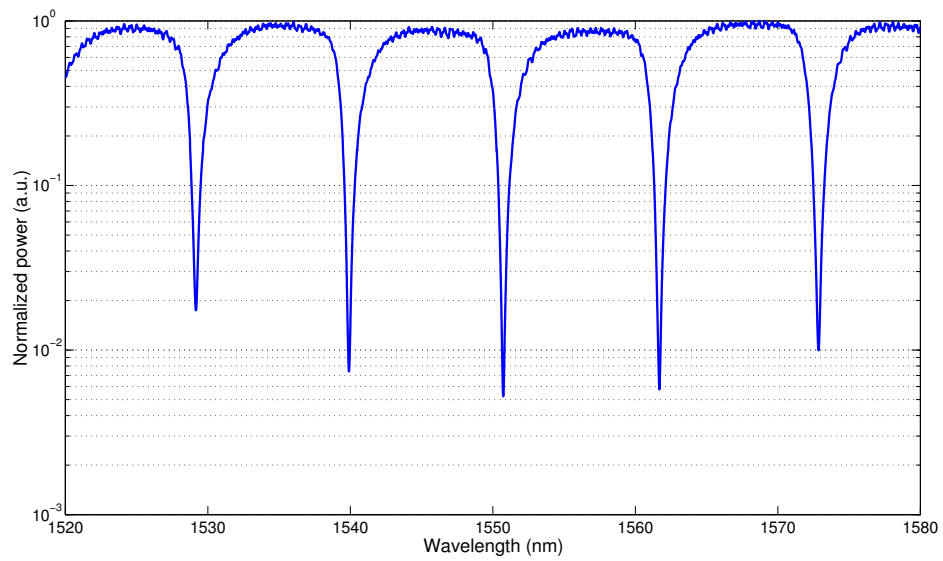


(b)

Figure 4.8: (a) Optical micrograph of a BCB microring resonator with a radius of 15 μm and a coupling gap of -0.6 μm, and (b) its measured transmission spectrum of the BCB device.



(a)



(b)

Figure 4.9: (a) Optical micrograph of a BCB microracetrack with a radius of 15 μm , a straight section of 20 μm , and a coupling gap of -0.2 μm , and (b) its measured transmission spectrum.

4.4 Conclusions

In this chapter, BCB microring resonators in both add-drop and all-pass configurations have been demonstrated. The fabricated BCB microring add-drop filters with wide FSR and high finesse are low loss and compact. Using negative-gap coupling scheme, the resonators are critically coupled and the notch filters exhibit high extinction.

Chapter 5

Microring Lattices

5.1 Introduction

Photonic bandgap (PBG) structures have many interesting applications including bandpass and bandstop filtering [52], slow and fast light propagation [53], [54], structural dispersion engineering [55], and gap soliton formation in nonlinear media [56]. Microring arrays have emerged as a promising approach to the implementation of one-dimensional PBG. Recently serially coupled microrings of up to 11 or 12 resonators have been demonstrated in glass and polymers [57], [58]. A major drawback with these structures; however, is the requirement of extremely tight fabrication control and uniformity. Without additional efforts in cavity tuning, high transmission loss resulting from resonance mismatch makes serial coupling impractical for forming very long chains of resonators.

In this chapter, PBG lattices are implemented with parallel-cascaded microrings and demonstrate low-loss transmission through a periodic chain consisting of more than 100 resonators. Compared to the serial coupling scheme, the parallel-cascaded microring lattice is more robust because it is considerably less sensitive to fabrication variations in the microring resonances, gap dimensions, and periodic spacings [59]. Furthermore, because of the periodicity, only weak coupling between the waveguide and the microring is needed to achieve a wide bandgap, thus removing

the fabrication difficulty of patterning very narrow coupling gaps required for a single microring device of comparable bandwidth.

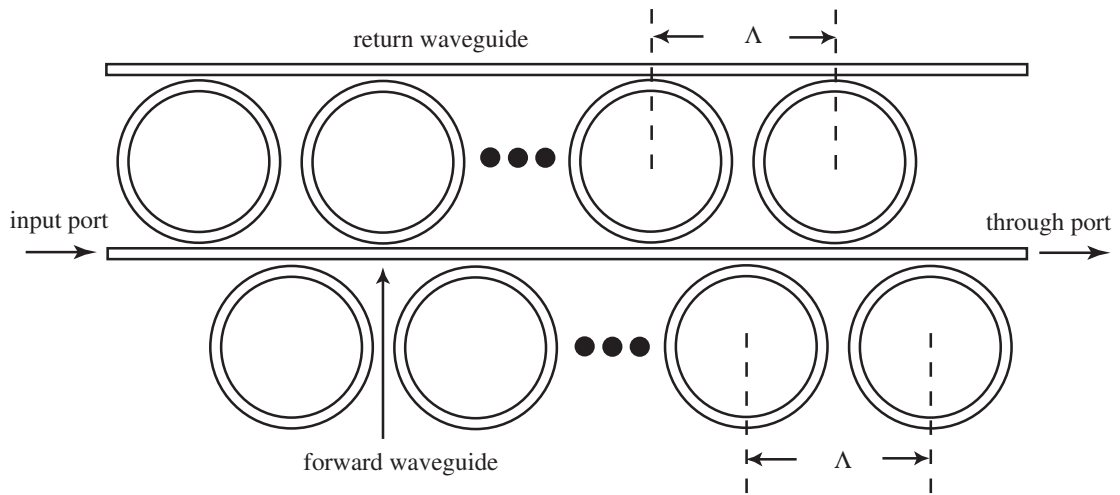
5.2 Theory

A schematic diagram of our parallel-cascaded microring lattice is shown in Fig. 5.1(a). The device consists of a forward waveguide periodically loaded on both sides by identical microring resonators. A return waveguide coupled to the top row of rings provides destructive feedback to the input signal within the stopband. Each period of the lattice, as shown in Fig. 5.1(b), consists of a top microring in the add-drop configuration and a bottom microring in the all-pass configuration, with the latter operating as a notch filter to provide additional signal extinction in the stopband.

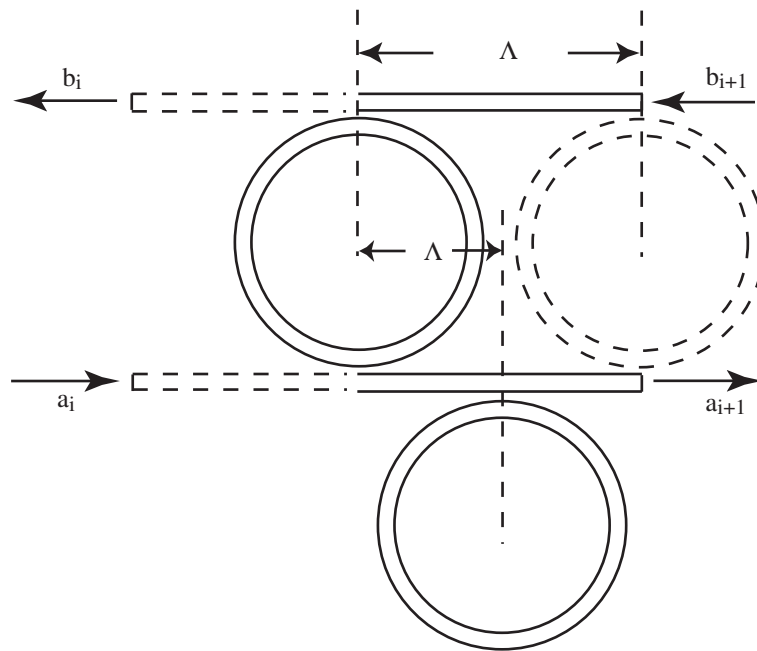
For a symmetric single-ring add-drop filter, Eqs (2.16) and (2.17) can be simplified to

$$T_{ad} = \frac{\tau(1 - a_{rt}e^{-j\phi})}{1 - \tau^2 a_{rt}e^{-j\phi}} \quad (5.1)$$

$$R_{ad} = \frac{-\kappa^2 a_{rt}^{1/2} e^{-j\phi/2}}{1 - \tau^2 a_{rt}e^{-j\phi}} \quad (5.2)$$



(a)



(b)

Figure 5.1: (a) Schematic diagram of a periodic microring lattice. (b) Components of a period.

The transmission of the all-pass filter T_{ap} is

$$T_{ap} = \frac{\tau - a_{rt} e^{-j\phi}}{1 - \alpha_{rt} e^{-j\phi}}. \quad (5.3)$$

The transfer matrix for each period M is obtained by cascading the transfer matrix of the waveguide propagation M_{wg} , add-drop filter M_{ad} , and all-pass filter M_{ap}

$$\begin{bmatrix} b_{i+1} \\ a_{i+1} \end{bmatrix} = M \begin{bmatrix} b_i \\ a_i \end{bmatrix} = M_{wg} M_{ap} M_{wg} M_{ad} \begin{bmatrix} b_i \\ a_i \end{bmatrix} \quad (5.4)$$

$$M_{wg} = \begin{bmatrix} e^{jk\Lambda/2} & 0 \\ 0 & e^{-jk\Lambda/2} \end{bmatrix} \quad (5.5)$$

$$M_{ap} = \begin{bmatrix} 1 & 0 \\ 0 & T_{ap} \end{bmatrix} \quad (5.6)$$

$$M_{ad} = \frac{1}{T_{ad}} \begin{bmatrix} 1 & -R_{ad} \\ R_{ad} & T_{ad}^2 - R_{ad}^2 \end{bmatrix} \quad (5.7)$$

where k is the propagation constant of the waveguide mode and Λ is the spacing between each period. After N microring periods

$$\begin{bmatrix} b_N \\ a_N \end{bmatrix} = M^N \begin{bmatrix} b_0 \\ a_0 \end{bmatrix} \equiv T \begin{bmatrix} b_0 \\ a_0 \end{bmatrix}. \quad (5.8)$$

The through port transmission of the lattice, T_{lat} , is given by

$$T_{lat} = \left. \frac{a_N}{a_0} \right|_{b_B=0} = t_{22} - \frac{t_{12}t_{21}}{t_{11}} \quad (5.9)$$

where t_{11} , t_{12} , t_{21} , and t_{22} are the elements of the transfer matrix T .

Simulation results on our fabricated lattice, with parameters described in next section, are shown in Fig. 5.2. to Fig. 5.4. Fig. 5.2 shows the stopband spectrum for several numbers of periods. Given the identical coupling efficient and round-trip loss in all the microrings, a lattice with more periods exhibits deeper extinction, steeper slope, and wider bandwidth. Compared to a single microring device, the 10-period lattice requires only one-tenth the coupling strength to achieve comparable bandwidth and a deeper extinction. Fig. 5.3 and Fig. 5.4 show the stopband width and transmission loss of the lattice, which is defined as the excess loss measured at the through port away from the stopband, as functions of period number and the coupling efficiency. With 4% round-trip loss in each microring and taking a 5 dB/cm propagation loss of the bus waveguides obtained by the cutback method into account, the 36-period lattice has a transmission loss less than 2 dB, suggesting the possibility of realizing microring arrays having lengths exceeding 100 periods for resonator-number-dependent PBG applications such as slow light propagation. In addition, the bandwidth of the 36-period device response can be significantly tuned by slightly changing the coupling strength.

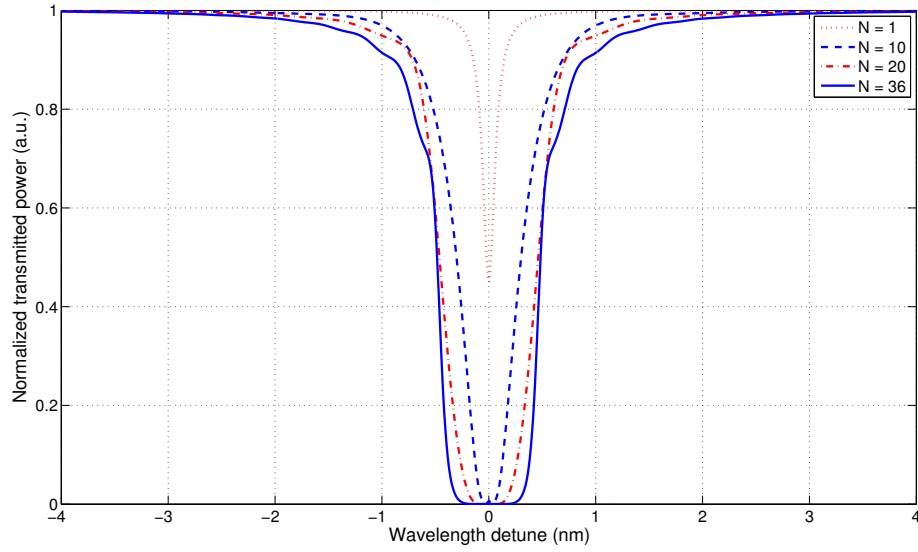


Figure 5.2: Theoretical response of the lattice with 1, 10, 20, and 36 periods where the ring resonators have 1% coupling efficiency and 4% round-trip loss.

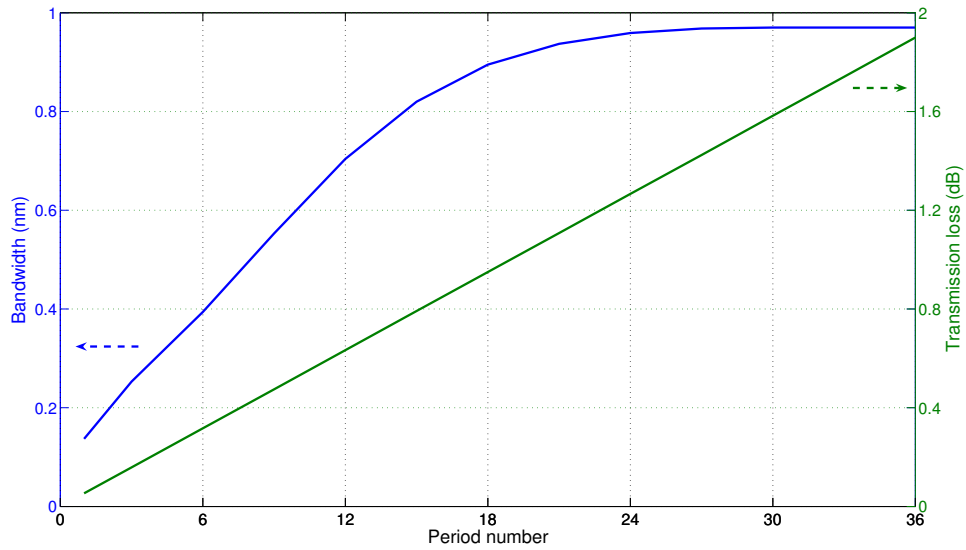


Figure 5.3: Stopband width and transmission loss of the lattice with 1% coupling efficiency and 4% loss.

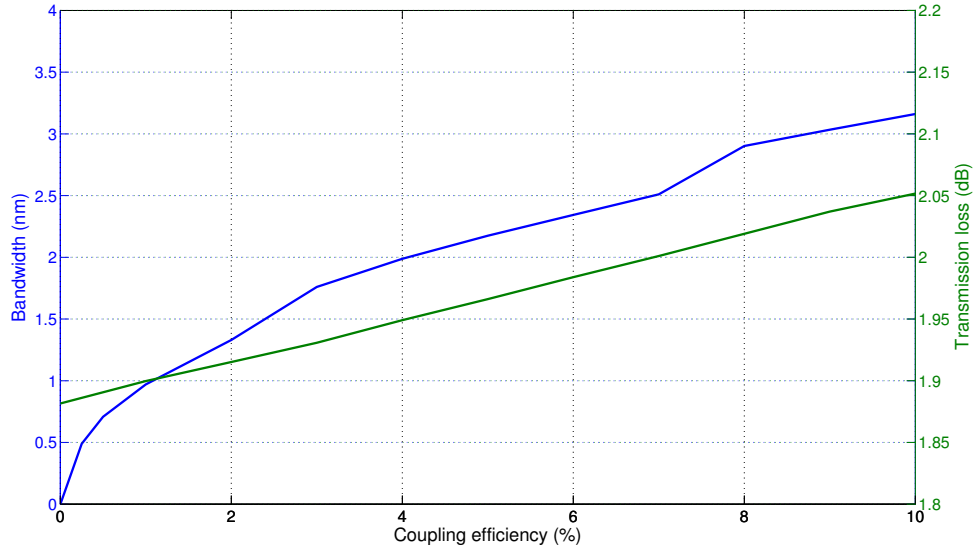


Figure 5.4: Stopband width and transmission loss of the 36-period lattice with 4% round-trip loss.

5.3 Device Characteristics

The device, as shown in Fig. 5.5, was fabricated in benzocyclobutene (BCB) polymer on a SiO_2 substrate. The microracetracks were designed to have a $10\text{-}\mu\text{m}$ radius, a $20\text{-}\mu\text{m}$ straight coupling section, and $0.6\text{-}\mu\text{m}$ coupling gaps. The periodic spacing Λ between the resonators was about half of the racetrack circumference L .

Eq (5.4) can be written as

$$\begin{bmatrix} b_{i+1} \\ a_{i+1} \end{bmatrix} = M \begin{bmatrix} b_i \\ a_i \end{bmatrix} = e^{j\beta\Lambda} \begin{bmatrix} b_i \\ a_i \end{bmatrix}, \quad (5.10)$$

where β is the Bloch propagation constant and the factor $e^{j\beta A}$ is the eigenvalue of the matrix [55]. Fig. 5.6 shows the calculated kL - βA diagram of an infinitely periodic structure. The through port transmission spectrum shows that bandgaps exist for kL equal to an integer multiple of 2π , which corresponds to a microring resonance. The measured TM-polarized spectral response at the through port after transmission through 36 periods is shown in Fig. 5.7. The device has a wide FSR of 14.2 nm, a stopband of 1.6 nm, and a maximum extinction of 25 dB. From the measurement, the extracted device has parameter values of 2% coupling efficiency and 4% round-trip loss, or 17 dB/cm, in the microracetrack. Compared to the averaged output power from BCB straight waveguides with the same length, the microring lattice has a measured excess loss of only 1.5 dB, which agrees with the theory within experimental uncertainties.

Fig. 5.8 is a fine scan of the bandgap at 1574 nm, showing a wide stopband of 200 GHz. The stopband shows an almost ideal flat bottom, despite fabrication defects in a few racetracks. Indeed, the simulated transmission spectrum of the periodic lattice without defects agrees well with the measurement, showing the robustness of the periodic structure.

Furthermore, Fig. 5.9 shows the transmission spectrum of a microring lattice consisting of 112 resonators (56 periods). The device has a FSR of 14.2nm, a maximum extinction of 25 dB, and a stopband of 4.8 nm. The microring lattice, compared to the averaged output power from straight waveguides, has a measured excess loss of 3 dB only, which well matches with the theory.

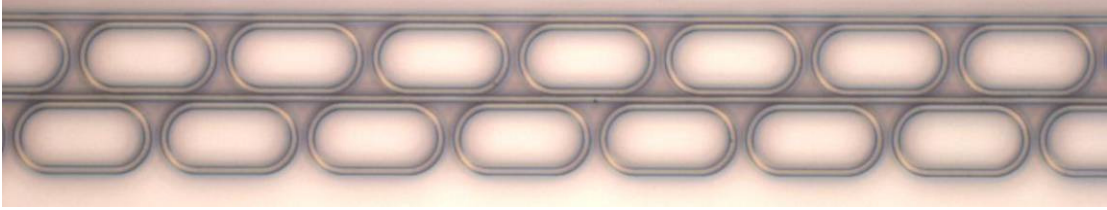


Figure 5.5: Optical micrograph on part of a 36-period BCB microring lattice.

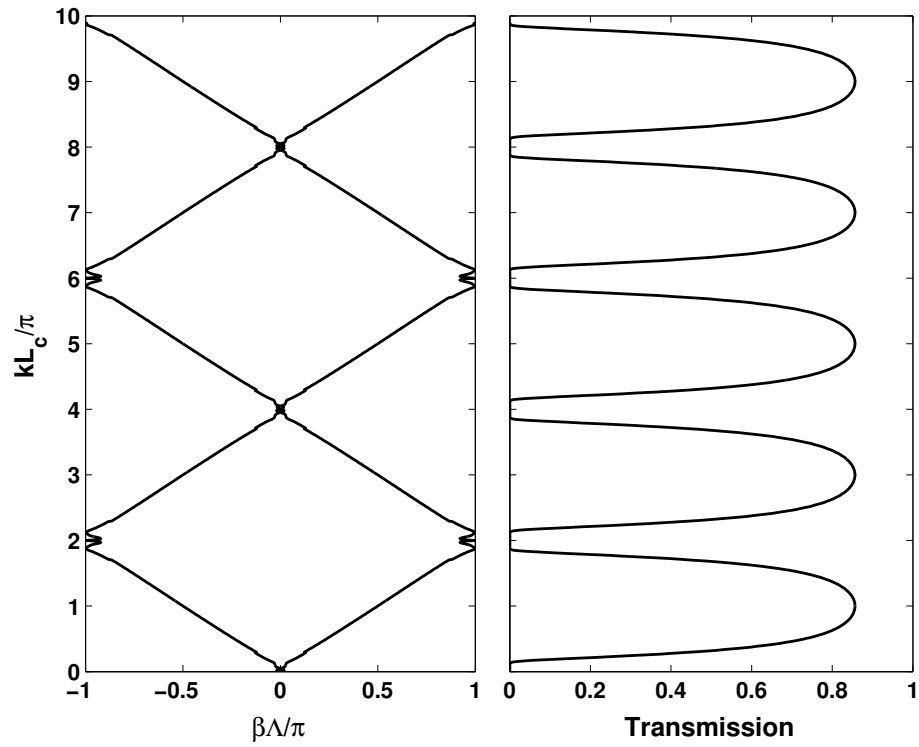


Figure 5.6: Calculated band diagram and the through port transmission spectrum of the device.

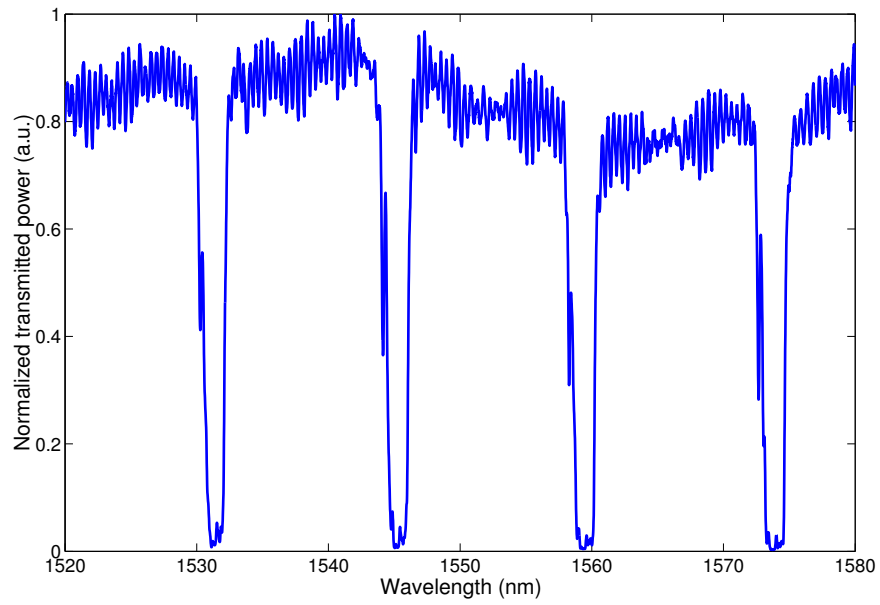


Figure 5.7: Transmission spectrum of a 36-period microring lattice.

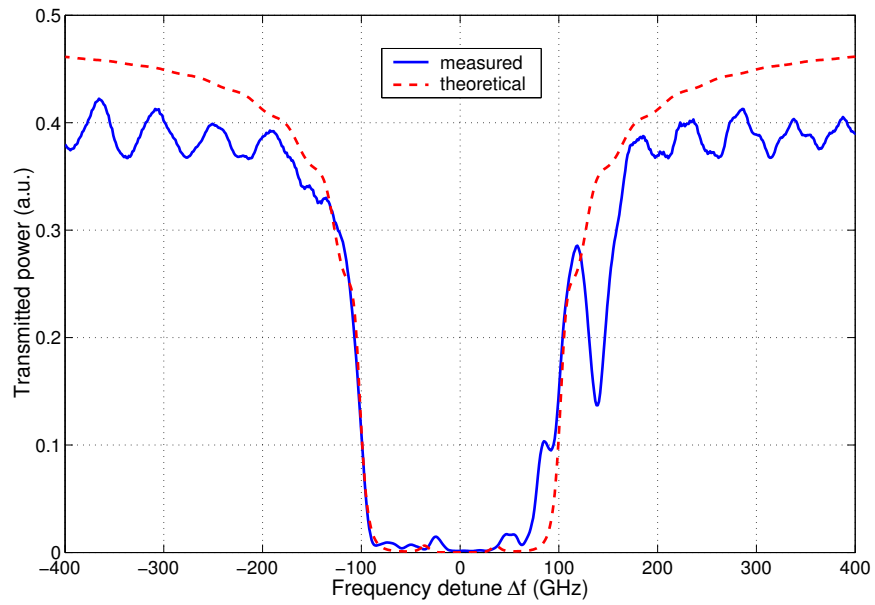


Figure 5.8: Measured and theoretical transmission spectra of the 36-period microring lattice.

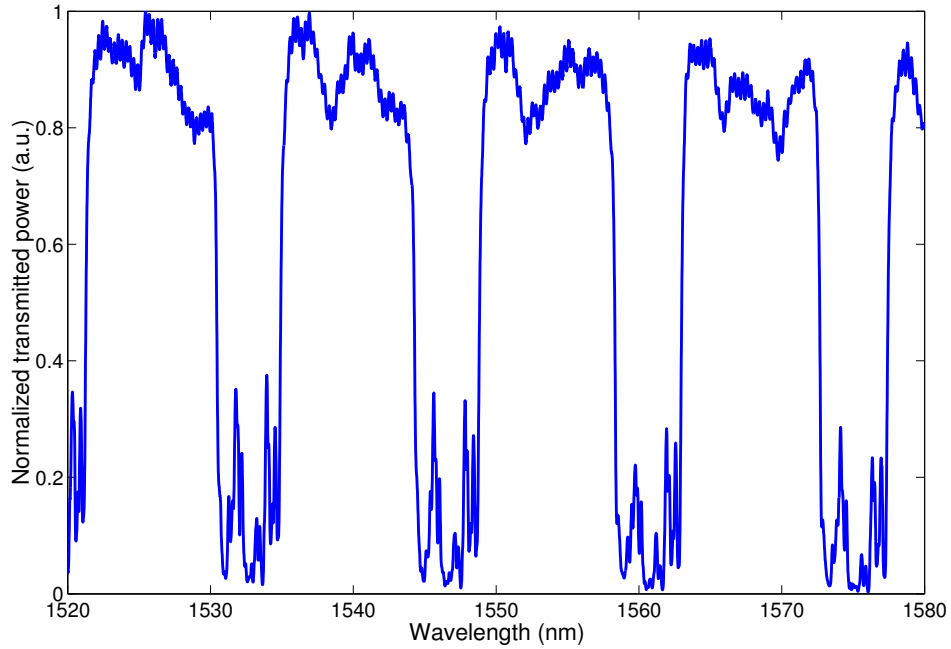


Figure 5.9: Transmission spectrum of a 56-period BCB microring lattice.

5.4 Conclusions

In summary, photonic lattices consisting of an array of parallel-cascaded microrings, the scheme considerably less sensitive to fabrication variations, have been demonstrated. Both microring lattices exhibit low transmission loss and a wide bandgap response without the requirement of a strong coupling efficiency by narrow coupling gaps. Furthermore, the parallel-cascaded microring scheme enables us to push the number of microrings in a device from single digit to triple digits, while preserving low propagation loss. The 36-period microring lattice shows an almost ideal flat bottom at stopband and can be used as a bandstop filter. The devices may

have potential applications in wideband filters, dispersion control, slow light propagation, and optical delay lines.

Chapter 6

Nonlinear Effects in Microring Resonators

6.1 Introduction

The application of microring resonators is not limited within the area of passive filters. For example, microring resonators can be actively controlled by electro-optic or thermo-optic effect as tunable filters [60], [61]. Optical pumping or electrical injection can change the loss or the gain of waveguides and makes the microrings as amplifiers and lasers [62], [63].

All-optical switching refers to the direct manipulation of optical signals without the need of intermediate conversion to electrical signals before switching takes place. The response time of all-optical switching by nonlinear optical effects can be as fast as in picoseconds or even femtoseconds [64], and its ultrafast speed fits the need of optical communication systems. While all-optical switching in microring devices can be demonstrated by using an external optical pumping on a microring [65], sending the pump into the microring and making use of the field enhancement in the resonator helps to significantly reduce the required switching power [66]. A few applications of all-optical switching in microring devices, such as time-division demultiplexing and logic operations [67]–[69], have been demonstrated.

In this chapter, the optical bistability in microring resonators is observed and its mechanic is investigated. This collaborative work was done with Dr. W. Cao, Dr.

W. Herman, and Dr. J. Goldhar at LPS. In addition, all-optical nonlinear switching in a microring lattice is investigated and demonstrated.

6.2 Thermal Tuning

The microring devices can be thermally tuned for a desired resonant wavelength. Fig. 6.1 shows the measured transmission spectra of a 56-period BCB microring lattice, which was placed on a thermo-electric temperature controller, at 15 °C and 50 °C. It can be seen that both the shape and the bandwidth of the stopband remain unchanged as a result of the temperature tuning. The increase of the temperature gives rise to a blue shift of the resonant wavelength at a rate of 0.134 nm/°C, corresponding to an effective refractive index change of $-1.35 \times 10^{-4}/^{\circ}\text{C}$. The change of effective refractive index is larger than the material dn/dT , $-8.6 \times 10^{-5}/^{\circ}\text{C}$, measured by a Metricon [71].

Using the thermo-optic effect may be the most intuitive way to make microring devices reconfigurable; however, the response time can be as slow as 1 ms [70], rendering the devices inappropriate for the high-speed applications.

6.3 Optical Bistability in Single Microring Resonator

6.3.1 Theory

Optical bistability arises from a combination of nonlinear optical interaction and a positive feedback [72]. Because of the field-induced change in refractive index,

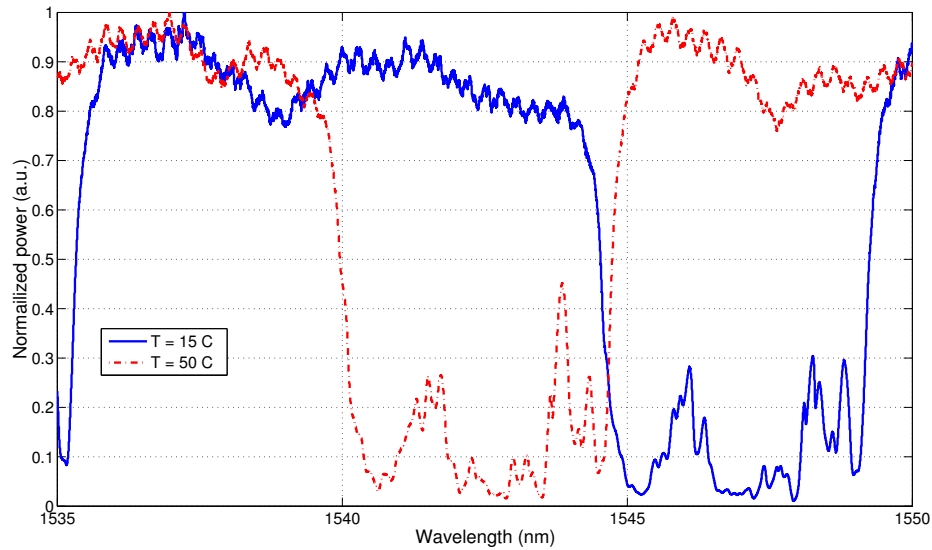


Figure 6.1: Measured transmission spectra of a 56-period BCB microring lattice at 15 °C and 50 °C.

the transmission of a nonlinear microring resonator depends on the input intensity [73], and the nonlinear transmission characteristics can be used for bistable operation.

In the up-tuning, the wavelength of the input beam moves towards a resonance, and the increased intensity in the microring changes the refractive index and shifts the resonance towards the input beam wavelength, leading to stronger intensity in the microring until the wavelengths of resonance and the input align. On the other hand, in the down-tuning, the wavelength of the input beam moves towards the resonance, but the resonance shifts away, keeping the input chasing until a critical wavelength.

From (2.16), the transmission at the drop port of the add-drop configuration is given by

$$|R_{ad}|^2 = \frac{\kappa^4 a_{rt}}{1 + \tau^4 a_{rt}^2 - 2\tau^2 a_{rt} \cos \phi} = \frac{\kappa^4 a_{rt}}{(1 - \tau^2 a_{rt})^2 + 4\tau^2 a_{rt} \sin^2(\phi/2)}. \quad (6.1)$$

Assuming optical Kerr effect is dominant and ignoring all other minor nonlinear effects [74], the wavelength-dependent phase contribution ϕ can be written as

$$\phi = \frac{2\pi}{\lambda} Ln = 2\pi L \frac{n_0 + \Delta n}{\lambda_0 + \Delta \lambda} = 2\pi L \frac{n_0 + n_2 I}{\lambda_0 + \Delta \lambda} = 2\pi L \frac{n_0(1 + n_2 I / n_0)}{\lambda_0(1 + \Delta \lambda / \lambda_0)}. \quad (6.2)$$

where n_0 is the usual weak-field refractive index, n_2 is the second-order refractive index characterizing the optical nonlinearity, and I is the intensity of the field in the microring. The approximated transmission is given by

$$|R_{ad}|^2 \cong \frac{\kappa^4 a_{rt}}{(1 - \tau^2 a_{rt})^2 + 4\tau^2 a_{rt} \left(\pi L \frac{n_0}{\lambda_0} \right)^2 \left[\frac{n_2 I}{n_0} - \frac{\Delta \lambda}{\lambda_{00}} \left(1 + \frac{n_2 I}{n_0} \right) \right]^2}. \quad (6.3)$$

6.3.2 Experiment

The BCB microring resonator used in the experiment has a radius of 20 μm , a FSR of 11, and a finesse F of 57. The input was a continuous-wave (CW) laser beam with an average power of 5 mW. Fig. 6.2 shows the drop-port power with respect to

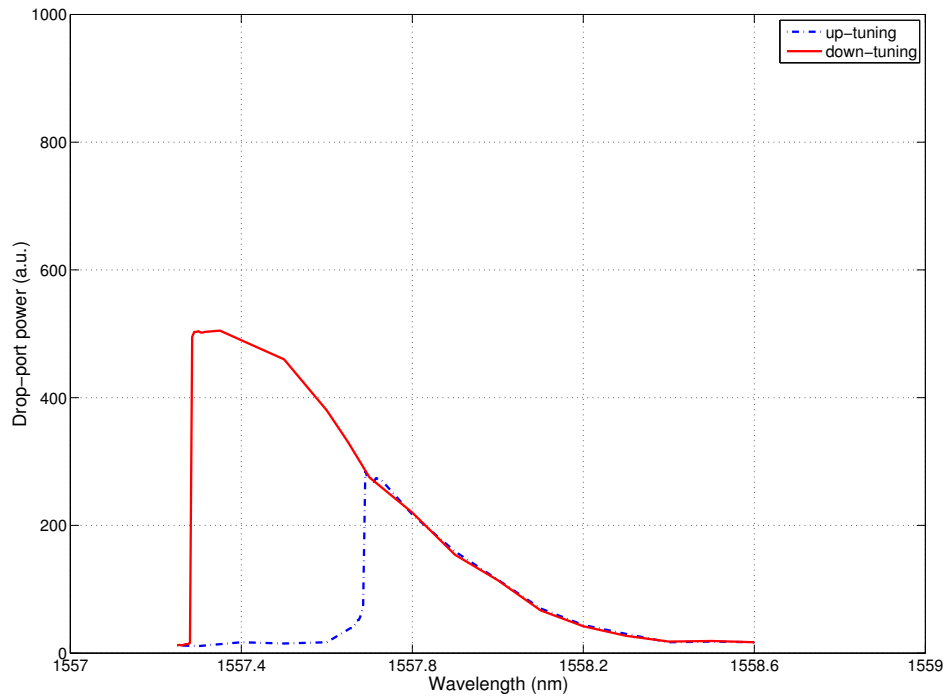


Figure 6.2: Hysteresis cycle of the optical bistability in a BCB microring resonator.

the wavelength. When the wavelength of the input was initially up-tuned through the microring resonance, the intensity-induced blue shift in the resonance and the positive feedback loop effect resulted in a rapid increase in transmission. The on-switching response in frequency domain is less than 5 pm. When the laser wavelength was down-tuned, the strong intensity in the microring kept changing the refractive index with an even higher transmission after on-switching point was passed. Finally, when

the laser wavelength was far away from the original resonance, the transmitted intensity caused a rapid attenuation in positive feedback loop. The off-switching

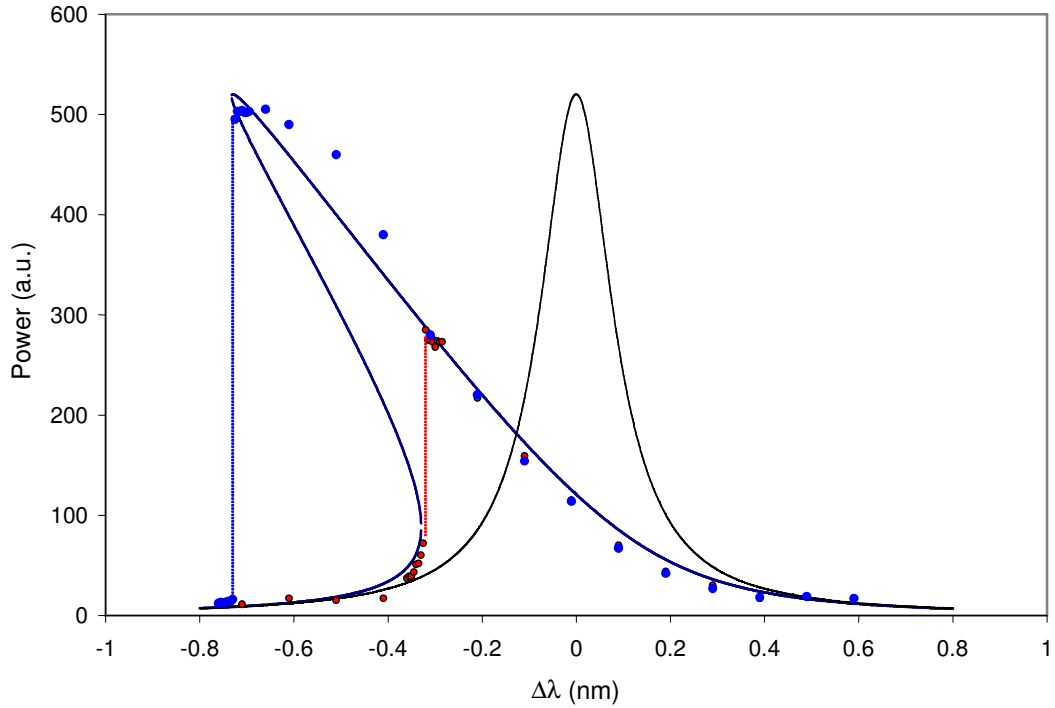


Figure 6.3: Simulated transmission of the optical bistability in a microring resonator (from Dr. W. Herman).

response is also less than 5 pm.

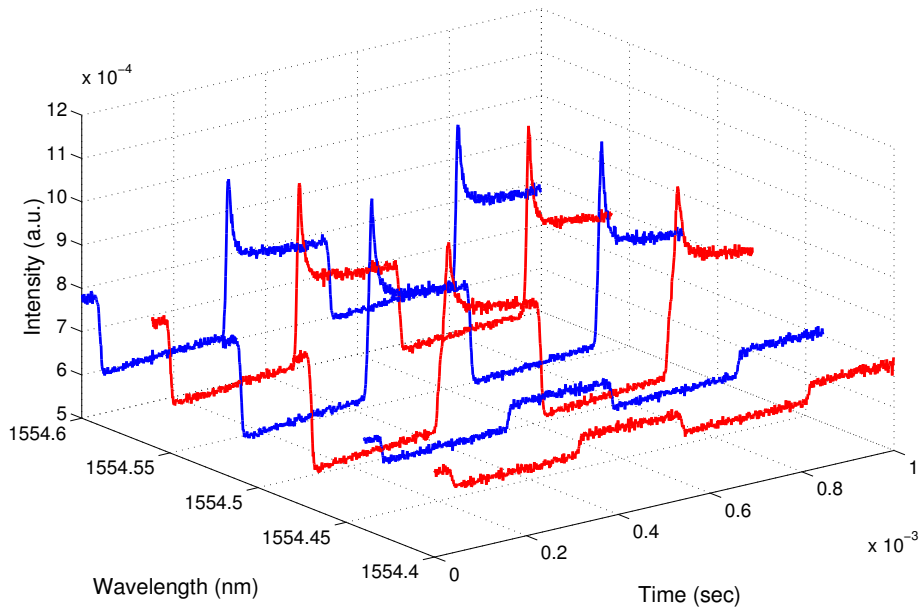
Fig. 6.3 shows a simulated transmission of the device. The simulation model gives rise to a maximum refractive index change of -4.7×10^{-4} , which leads to a resonance shift of 0.7 nm.

6.3.3 Mechanism for Optical Bistability in BCB Microring Resonators

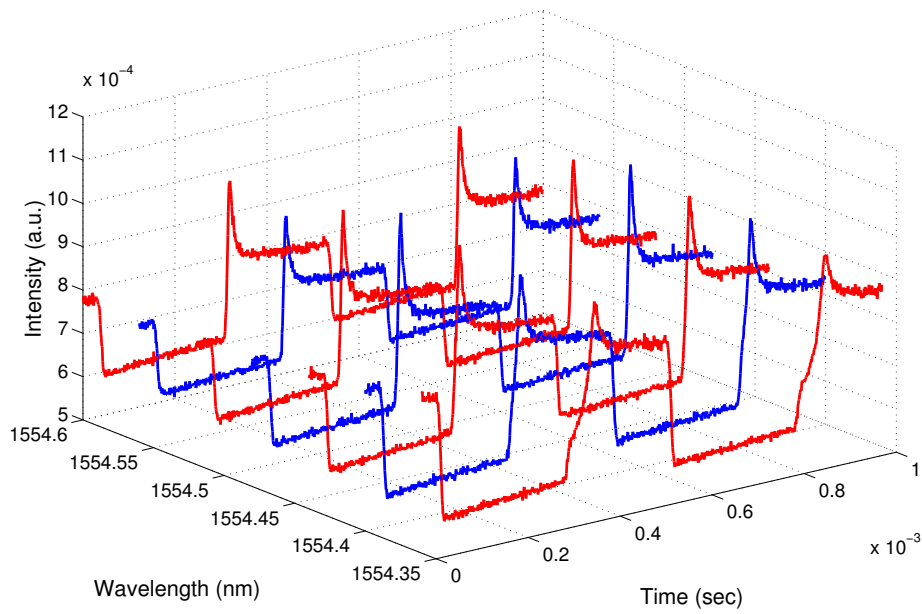
The optical bistability takes place only in microring resonators with an undercut cladding. No optical bistability is observed from microring resonators with a regular channel waveguide structure even microring characteristics are close. The issue raised the attention to the mechanism responsible for the optical bistability.

In the perspective of the waveguide structure, the BCB (with an absorption coefficient of 0.3 cm^{-1} at 1550 nm [75]) waveguide core in undercut cladding structure has a smaller contact area with the SiO_2 cladding and a larger contact area with the air than the BCB waveguide core in a regular channel waveguide. Given the thermal conductivity of the BCB (0.24 W/K m) is about ten times larger than one of the air (0.025 W/K m) but less than one-fifth of the thermal conductivity of the SiO_2 (1.38 W/K m) [76], [77], the heat generated by high optical intensity in the resonator may be bounded in the BCB and thermally change its refractive index in former case, while in the latter case the heat can be relatively easily sent into SiO_2 and dissipated.

Rather than using a CW beam, the input laser was externally modulated at a low frequency by either an optical chopper or a function generator. The BCB microring resonator used in the experiment has a radius of $10 \text{ }\mu\text{m}$, a FSR of 24, and a finesse F of 285. Fig 6.4 shows the measured power at the drop port of the microring device with a modulated input square wave at the frequency of 2 KHz . In addition to the optically bistable hysteresis in the frequency domain, it also shows waveform distortions for wavelengths close to the resonant wavelength of the microring. The time constant of the bistability τ_b can be found by



(a)



(b)

Figure 6.4: Measured drop-port power from a microring device with wavelength (a) up-tuning and (b) down-tuning.

$$\frac{d\phi}{dt} = \frac{\phi_0 - \phi}{\tau_b} + KI_{ring}, \quad (6.4)$$

where ϕ_0 is the wavelength-dependent phase contribution with the usual refractive index n_0 and K is the coefficient for the intensity in the microring resonator I_{ring} . I_{ring} is given by

$$I_{ring} = \frac{\kappa^2}{1 + \tau^4 a_{rt}^2 - 2\tau^2 a_{rt} \cos \phi} I_{in}. \quad (6.5)$$

An estimate of the time constant from model fitting is 70 μ s. Moreover, the output waveform distortion decreases as the modulating frequency increases. The input and the output waveform coincide at the frequency of 50 KHz, suggesting the thermal-optic effect is responsible for the optical bistability.

6.4 All-Optical Nonlinear Switching in Microring Lattice

A BCB mirroring lattice consisting of 56 periods was used in the experiment of high-speed, all-optical switching. The pump pulse width, which is shorter than the cavity lifetime of the microring lattice, was about 100 ps for high instantaneous pump energy. It is necessary to know the field enhancement factor FE of each resonator in the lattice.

6.4.1 Analysis on Field Enhancement Factor

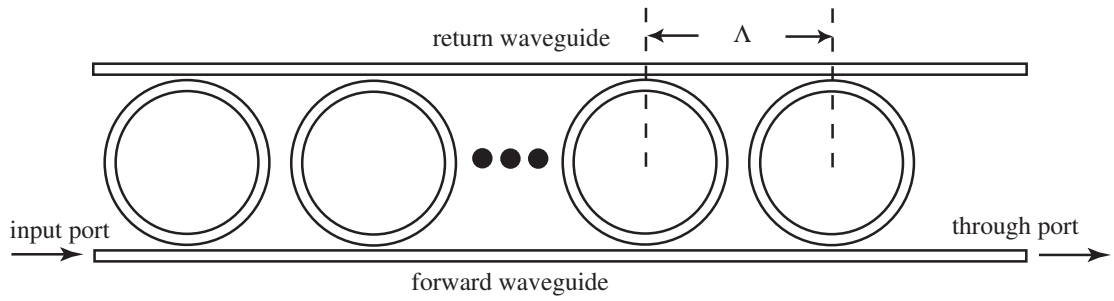
A schematic diagram of the single-row parallel-cascaded microring lattice is shown in Fig. 6.5(a). The device consists of a forward waveguide periodically loaded with identical microring resonators. A return waveguide coupled to the other side of the microrings provides feedback to microrings of previous periods. Fig. 6.5(b) shows the double-row parallel-cascaded microring lattice, whose forward waveguide is periodically loaded with microrings on both sides. Each period of the lattice, as shown in Fig. 6.5(c), can be regarded as consisting of one microring in the add-drop configuration for single-row microring lattices, plus the other microring in the all-pass configuration for double-row microring lattices.

For a single-ring add-drop filter, at time t , the fields circulating inside the ring resonator of period i at the forward coupling section $E_{i,RF}$ and at the return coupling section $E_{i,RR}$ are given by

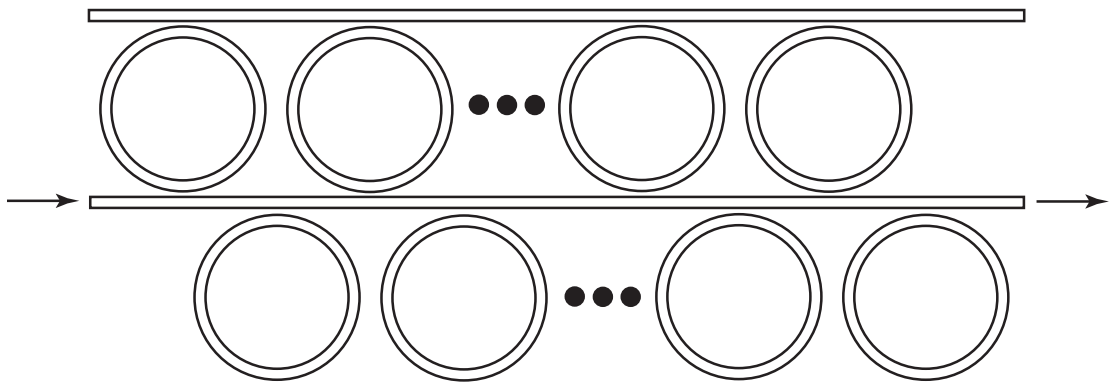
$$E_{i,RF}(t) = -j\kappa E_{i,I}(t) + \alpha_t^{1/2} e^{-j\phi/2} E_{i,RR}(t) \quad (6.6)$$

$$E_{i,RR}(t) = -j\kappa E_{i,A}(t) + \alpha_t^{1/2} e^{-j\phi/2} E_{i,RF}(t). \quad (6.7)$$

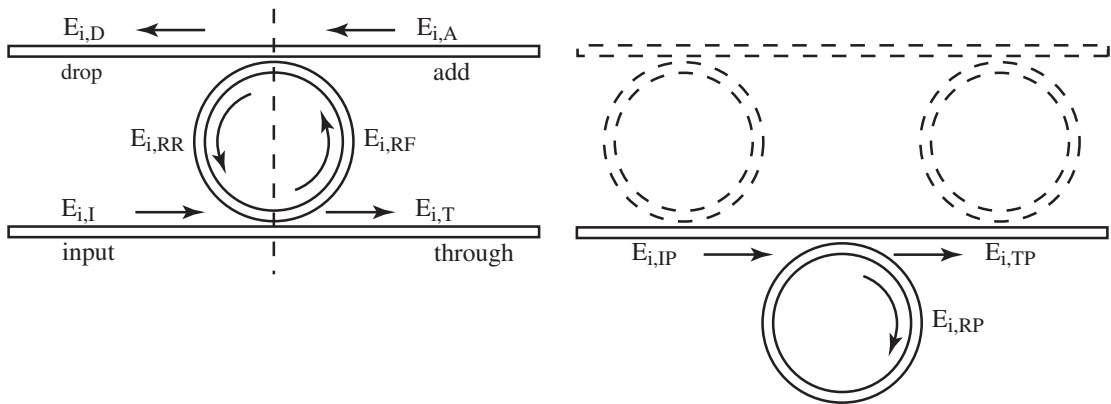
The fields at the input port $E_{i,I}$ and the add port $E_{i,A}$ are related to adjacent ring resonators



(a)



(b)



(c)

Figure 6.5: Schematic diagram of (a) a single-row microring lattice, (b) a double-row microring lattice, and (c) components in one period of a single-row and a double-row microring lattice, respectively.

$$E_{i,I}(t) = e^{-jk\Lambda} E_{i-1,T}(t) \quad (6.8)$$

$$E_{i,A}(t) = e^{-jk\Lambda} E_{i+1,D}(t) \quad (6.9)$$

The fields at the through port $E_{i,T}$ and the drop port $E_{i,D}$ are

$$E_{i,T}(t) = -j\kappa\alpha_{rt}^{1/2} e^{-j\phi/2} E_{i,RR}(t) + \tau E_{i,I}(t) \quad (6.10)$$

$$E_{i,D}(t) = -j\kappa\alpha_{rt}^{1/2} e^{-j\phi/2} E_{i,RF}(t) + \tau E_{i,A}(t). \quad (6.11)$$

The field enhancement factor FE of each resonator in the add-drop configuration, defined as the ratio of the field circulating inside the ring $E_{i,RR}$ to the field at the first input port $E_{i,I}$, can be obtained numerically by iterations.

For a single-ring all-pass filter, the electric field circulating inside the ring resonator of period i is

$$E_{i,RP}(t) = -j\kappa E_{i,IP}(t) + \tau\alpha_{rt} e^{-j\phi} E_{i,RP}(t). \quad (6.12)$$

The fields at the input port $E_{i,IP}$ and the through port $E_{i,TP}$ are

$$E_{i,IP}(t) = e^{-jk\Lambda/2} E_{i,T}(t) \quad (6.13)$$

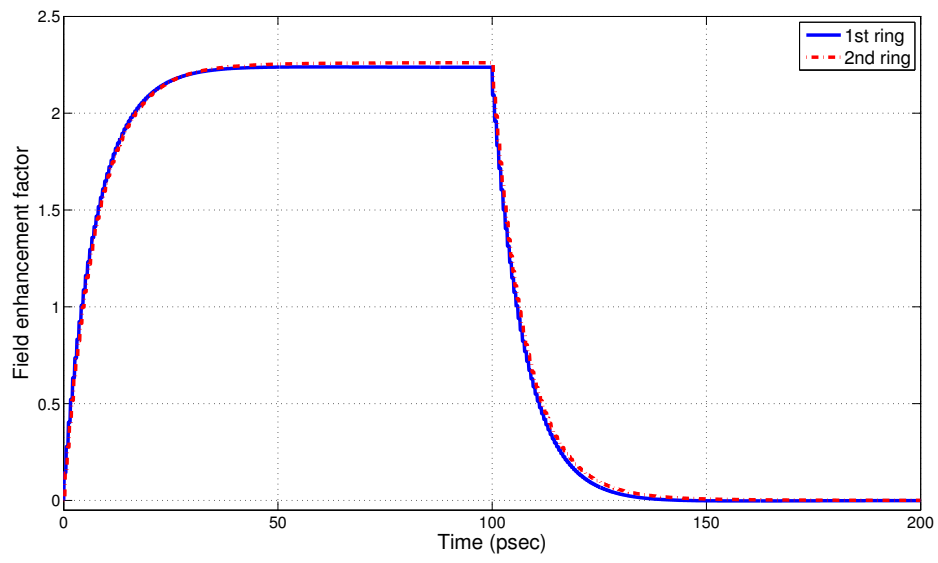
$$E_{i,TP}(t) = -j\kappa\alpha_{rt} e^{-j\phi} E_{i,RP}(t) + \tau E_{i,IP}(t). \quad (6.14)$$

For a double-row microring lattice, the electric field at the input port $E_{i,I}$ is given by

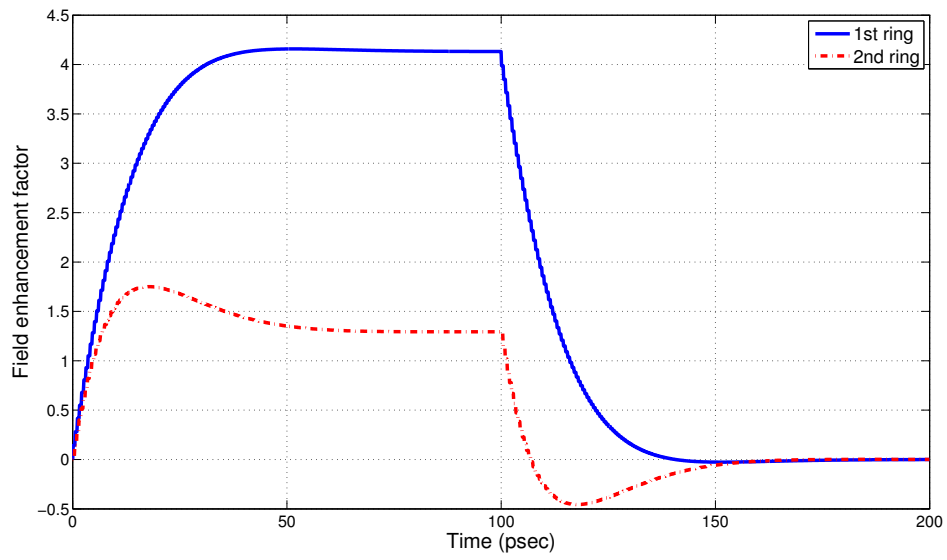
$$E_{i,I}(t) = e^{-jk\Lambda/2} E_{i-1,TP}(t). \quad (6.15)$$

Considering all equations above, the *FE* of each resonator in all-pass configuration is the ratio of $E_{i,RP}$ to $E_{I,I}$.

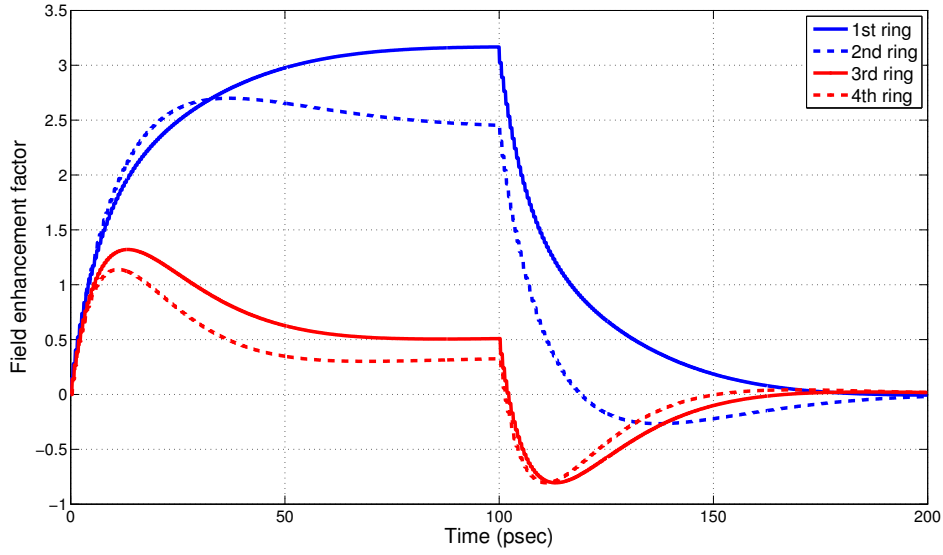
The dynamic *FE* of the microring lattice based on a 100-ps width pulse at input is simulated and shown in Fig. 6.6. The microring parameters used in simulation are $\kappa = 16\%$ and $a_{rt} = 98\%$. The *FE* of a 2-period single-row lattice with Λ equivalent to half of L is shown in Fig. 6.6(a). The *FE* is about 2.3 for both microrings. It is smaller than the *FE* of 3.6 for the single ring in an add-drop filter, because the feedback field from the second ring destructively interferes with the field circulating in the first ring. Fig. 6.6(b) shows the *FE* is 4.3 for the first ring and only 1.3 for the second in a 2-period single-row lattice with Λ equivalent to three-quarters of L . The feedback field from the second ring constructively interferes with the field in the first ring, but the increasing field in the first ring interacts with the input pulse and suppresses the field at through port, which subsequently reduces the field coupled into the second ring. Fig. 6.6(c) shows the *FE* in the microrings of a 2-period double-row lattice with Λ equivalent to half of L . The *FE* is 3.2 and 2.5 for microrings in the first period but 0.5 and 0.3 for microrings in the second period. Furthermore, the cavity charging time is about 50 ps for all microrings.



(a)



(b)



(c)

Figure 6.6: The dynamic field enhancement factor of a 2-period double-row microring lattice with (a) Λ equivalent to one-half of L and (b) Λ equivalent to three-quarters of L . (c) The dynamic field enhancement factor of a 2-period double-row microring lattice with Λ equivalent to one-half of L .

6.4.2 Experiment

The device used in the switching experiment, as shown in Fig. 6.7, was a BCB double-sided microring lattice with 56 periods. The transmission spectrum of the microring lattice, which exhibits a low transmission loss of only 3 dB after 56 periods, was previously shown in Fig. 5.9.

The experimental setup used to demonstrate switching by pump and probe method in a microring lattice is shown in Fig. 6.8. The pump signal, set to microring



Figure 6.7: Optical micrograph of a 56-period BCB microring lattice used in the experiment.

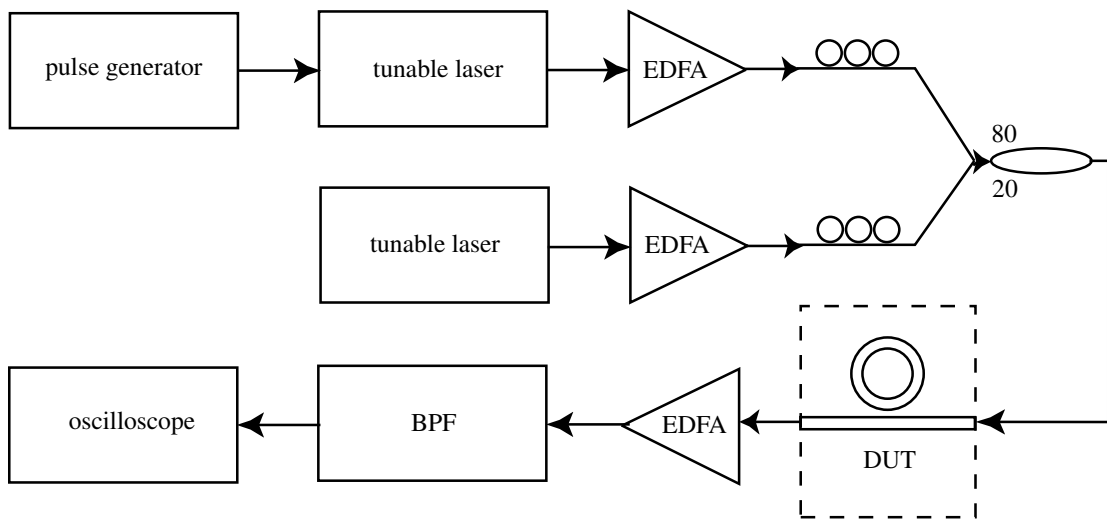


Figure 6.8: Experimental setup for pump-and-probe method.

resonance at 1533 nm, consisted of a laser diode which was externally modulated to produce a 100-ps pump pulse with a 32-MHz repetition rate. The CW probe signal tuned to the edge of the next band was combined with the probe signal through an 80/20 fiber coupler and sent into the input of the lattice. The output signal was amplified and the probe signal was distinguished by a bandpass filter and collected by

a 50-GHz oscilloscope with a 45-GHz photodetector. Fig. 6.9 shows the output probe signals with wavelength at the edges of the band. The red shift of the resonant wavelength resulting from the refractive index change leads to a dip response for probe at 1548.9 nm and a peak response for probe at 1544.5 nm. The switching time of the device is about 60 ps.

Fig. 6.10 shows the theoretical *FE* of first 10 rings in a 56-period microring lattice. Only the first 6 rings have the *FE* greater than 0.1 after cavity charging time, although the instantaneous *FE* of 8 rings can be greater than 0.5, as shown in Fig. 6.11. In other words, most rings contribute little to the nonlinear switching, excluding the ones in the first few periods. The estimated resonance shift caused by the high-power pulse is about 0.05 nm and the corresponding BCB refractive index change of 5×10^{-5} , leading to an estimated nonlinear refractive index n_2 of BCB about $3.1 \times 10^{-15} \text{ cm}^2/\text{W}$.

The other way to obtain the nonlinear refractive index n_2 is to measure the third-order nonlinear optical susceptibility $\chi^{(3)}$ from a BCB thin film by degenerate four-wave mixing (DFWM) technique with a phase grating [78], and then the n_2 is given by [74]

$$n_2(\text{cm}^2 / \text{W}) = \frac{12\pi^2}{n_0^2 c} 10^7 \chi^{(3)}(\text{esu}) = \frac{0.0395}{n_0^2} \chi^{(3)}(\text{esu}) . \quad (6.13)$$

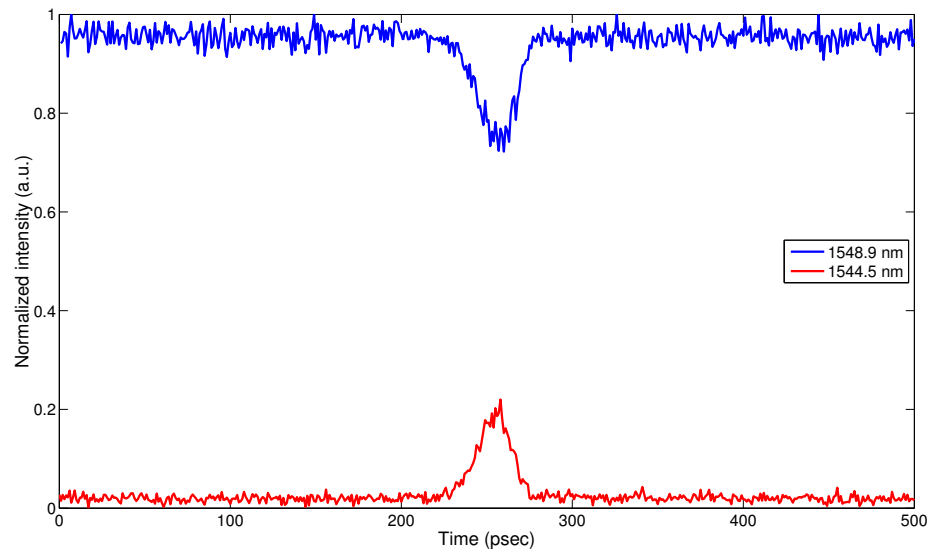


Figure 6.9: Measured response of probe signal.

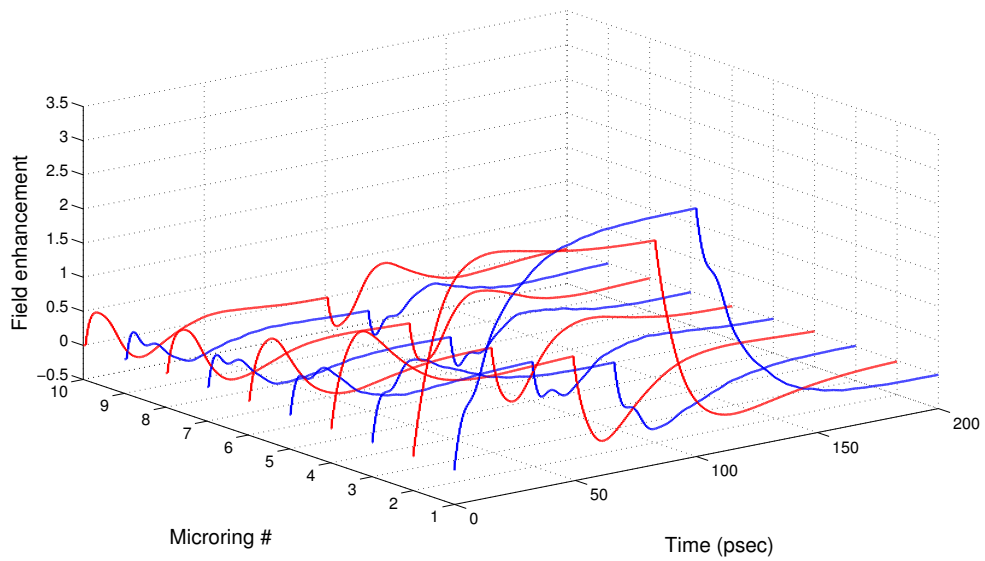


Figure 6.10: Theoretical dynamic FE of the rings in a 56-period double-row microring lattice.

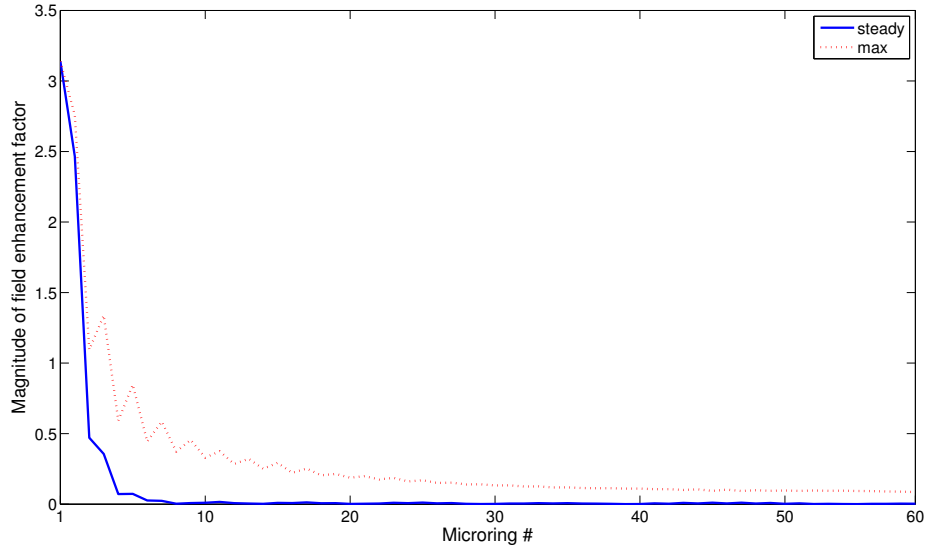


Figure 6.11: The FE of the microrings after cavity charging time and at the maximum. Microrings in the 31st period and after are neglected because of their little contribution to the switching.

The $\chi^{(3)}$ of BCB obtained by my colleague at LPS, Dr. W. Cao, is 2.1×10^{-13} esu, which corresponds to the n_2 of $3.5 \times 10^{-15} \text{ cm}^2/\text{W}$ and echoes with the number obtained from nonlinear switching of BCB microring lattice.

6.5 Conclusions

In summary, optical bistability in BCB microring resonators as a result of thermo-optic effect has been observed. The switching time is about 100 μs . In addition, the dynamics of the field enhancement factor in parallel-cascaded microring

lattices has been investigated and all-optical nonlinear switching in a 56-period double-row microring lattice on BCB has been demonstrated. The switching time of the nonlinear optic effect in the microring lattice is 60 ps. By the switching experiment, the estimated nonlinear refractive index of BCB is $3.1 \times 10^{-15} \text{ cm}^2/\text{W}$, which matches the n_2 of BCB obtained by DFWM technique.

Chapter 7

Conclusions

7.1 Achievements

In this work, the single-mode BCB waveguides and microring resonators were designed and fabricated. The BCB microring devices were demonstrated as add-drop filters and notch filters with a negative coupling gap. The microring resonators, which could be as small as 5 μm in radius, meet the size requirement for photonic VLSI and exhibit a high out-of-band rejection, high extinction as well as a high finesse.

In addition, BCB microring lattices were fabricated and demonstrated as bandstop filters. The parallel-cascaded microring scheme enables us to push the number of microrings in a device from single digit to triple digits, while preserving an extremely low propagation loss.

Finally, the optical bistability due to thermal effect was observed in single-microring resonators. Field-enhanced nonlinear switching was demonstrated in a BCB microring lattice. The switching speed, limited by the finesse of the device, is about 60 ps.

7.2 Future Directions

The next goal of microring research would focus on exploring applications on multiple microrings; for example, the investigation of slow light in microring lattices

and ring of rings, where a few microring resonators are located within one mother microring resonator.

On the other hand, in the material perspective, BCB is proven to be a polymer with a weak optical nonlinearity. However, BCB has already opened a door for polymer microring application. With the further development of high nonlinear polymers and the more advanced fabrication technology, polymer microring resonators will play an important role in photonic circuits as well as the entire WDM networks.

Appendix A

Field Enhancement Factor in Lossless Microring Resonators

It was shown in chapter 2 that the lower the round-trip loss, the higher the field enhancement of a microring resonator. It seems puzzling that, according to Fig. 2.7, the field enhancement factor becomes infinite while no coupling occurs in lossless microrings. From Eqs. (2.18) and (2.19), the field enhancement factor of a lossless microring can be written as

$$\lim_{\kappa \rightarrow 0} FE_{ap} \Big|_{a_{rt}=1} = \lim_{\kappa \rightarrow 0} \frac{\kappa}{1-\tau} = \lim_{\kappa \rightarrow 0} \frac{\kappa}{1-(1-\kappa^2)^{1/2}} \quad (\text{A.1})$$

$$\lim_{\kappa \rightarrow 0} FE_{ad} \Big|_{a_{rt}=1} = \lim_{\kappa \rightarrow 0} \frac{\kappa}{1-\tau^2} = \lim_{\kappa \rightarrow 0} \frac{\kappa}{1-(1-\kappa^2)} = \lim_{\kappa \rightarrow 0} \frac{1}{\kappa} \rightarrow \infty. \quad (\text{A.2})$$

Use L'hospital's Rule so FE_{ap} can be written as

$$\lim_{\kappa \rightarrow 0} FE_{ap} \Big|_{a_{rt}=1} = \lim_{\kappa \rightarrow 0} \frac{\kappa}{1-(1-\kappa^2)^{1/2}} = \lim_{\kappa \rightarrow 0} \frac{1}{\kappa(1-\kappa^2)^{-1/2}} \rightarrow \infty. \quad (\text{A.3})$$

On the other hand, their cavity lifetime is

$$\tau_{ph,ap} = \lim_{\kappa \rightarrow 0} \frac{\pi n_{eff} L (\alpha_{rt})^{1/2}}{c (1-\alpha_{rt})} \Big|_{a_{rt}=1} = \lim_{\tau \rightarrow 1} \frac{\pi n_{eff} L (\alpha_{rt})^{1/2}}{c (1-\alpha_{rt})} \Big|_{a_{rt}=1} \rightarrow \infty \quad (\text{A.4})$$

$$\tau_{ph,ad} = \lim_{\kappa \rightarrow 0} \frac{\pi m_{eff} L}{c} \frac{\alpha_{rt}^{1/2}}{1 - \tau^2 a_{rt}} \Big|_{a_{rt}=1} = \lim_{\tau \rightarrow 1} \frac{\pi m_{eff} L}{c} \frac{\alpha_{rt}^{1/2}}{1 - \tau^2 a_{rt}} \Big|_{a_{rt}=1} \rightarrow \infty, \quad (\text{A.5})$$

which implies the steady state can never be achieved.

Bibliography

- [1] G. Keiser, *Optical Fiber Communications*, 3rd ed.: McGraw-Hill, 2000.
- [2] E. A. J. Marcatili, “Bends in optical dielectric guides,” *The Bell System Technical Journal*, vol. 48, no. 7, pp. 2103–2132, 1969.
- [3] L. F. Stokes, M. Chodorow, and H. J. Shaw, “All-single-mode fiber resonator,” *Optics Letters*, vol. 7, no. 6, pp. 288–290, 1982.
- [4] J. Haavisto and G. A. Pajer, “Resonance effects in low-loss ring waveguides,” *Optics Letters*, vol. 5, no. 12, pp. 510–512, 1980.
- [5] R. Ulrich and H. P. Weber, “Unidirectional thin-film ring laser,” *Applied Physics Letters*, vol. 20, no. 1, pp. 38–40, 1972.
- [6] B. E. Little, J. S. Foresi, G. Steinmeyer, E. R. Thoen, S. T. Chu, H. A. Haus, E. P. Ippen, L. C. Kimerling, and W. Greene, “Ultra-compact Si-SiO₂ microring resonator optical channel dropping filters,” *IEEE Photonics Technology Letters*, vol. 10, no. 4, pp. 549–551, 1998.
- [7] B. E. Little, S. T. Chu, H. A. Haus, J. Foresi, and J.-P. Laine, “Microring resonator channel dropping filters,” *Journal of Lightwave Technology*, vol. 15, no. 6, pp. 998–1005, 1997.
- [8] S. T. Chu, B. E. Little, W. Pan, T. Kaneko, S. Sato, and Y. Kokubun, “An eight-channel add-drop filter using vertically coupled microring resonators over a cross grid,” *IEEE Photonics Technology Letters*, vol. 11, no.6, pp. 691–693, 1999.

- [9] B. E. Little, H. A. Haus, J. S. Foresi, L. C. Kimerling, E. P. Ippen, and D. J. Ripin, "Wavelength switching and routing using absorption and resonance," *IEEE Photonics Technology Letters*, vol. 10, no. 6, pp. 816–818, 1998.
- [10] H. W. Choi, C. W. Jeon, and M. D. Dawson, "InGaN microring light-emitting diodes," *IEEE Photonics Technology Letters*, vol. 16, no. 1, pp. 33–35, 2004.
- [11] C.-Y. Chao, W. Fung, and L. J. Huo, "Polymer microring resonators for biochemical sensing applications," *IEEE Journal of Selected Topics in Quantum Electronics*, vol. 12, no. 1, pp. 134–142, 2006.
- [12] C.-Y. Chao, S. Ashkenazi, S.-W. Huang, M. O'Donnell, and L. J. Guo, "High-frequency ultrasound sensors using polymer microring resonators," *IEEE Transactions on Ultrasonics, Ferroelectrics, and Frequency Control*, vol. 54, no. 5, pp. 957–965, 2007.
- [13] B. E. Little, S. T. Chu, W. Pan, and Y. Kokubun, "Microring resonator arrays for VLSI photonics," *IEEE Photonics Technology Letters*, vol. 12, no. 3, pp. 323–325, 2000.
- [14] Y. Hida, S. Imamura, and T. Izawa, "Ring resonator composed of low loss polymer waveguides at 1.3 μm ," *Electronics Letters*, vol. 28, pp. 1314–1316, 1992.
- [15] D. Rafizadeh, J. P. Zhang, S. C. Hagness, A. Taflove, K. A. Stair, S. T. Ho, and R. C. Tiberio, "Waveguide-coupled AlGaAs/GaAs microcavity ring and disk resonators with high finesse and 21.6 nm free spectral range," *Optics Letters*, vol. 22, pp. 1244–1246, 1997.

- [16] B. E. Little, S. T. Chu, W. Pan, D. Ripin, T. Kaneko, Y. Kokubun, and E. P. Ippen, "Vertically coupled glass microring resonator channel dropping filters," *IEEE Photonics Technology Letters*, vol. 11, no.2, pp. 215–217, 1999.
- [17] S. T. Chu, P. Wugan, S. Suzuki, B. E. Little, S. Sato, and Y. Kokubun, "Temperature insensitive vertically coupled microring resonator add/drop filters by means of a polymer overlay," *IEEE Photonics Technology Letters*, vol. 11, no. 9, pp. 1138–1140, 1999.
- [18] R. Grover, P. P. Absil, V. Van, J. V. Hryniewicz, B. E. Little, O. King, L. C. Calhoun, F. G. Johnson, and P.-T. Ho, "Vertically coupled GaInAsP–InP microring resonators," *Optics Letters*, vol. 26, no. 8, pp. 506–508, 2001.
- [19] R. Grover, T. A. Ibrahim, T. N. Ding, Y. Leng, L.-C. Kuo, S. Kanakaraju, K. Amarnath, L. C. Calhoun, and P.-T. Ho, "Laterally coupled InP-based single-mode microracetrack notch filter," *IEEE Photonics Technology Letters*, vol. 15, no. 8, pp. 1082–1084, 2003.
- [20] V. Van, P. P. Absil, J. V. Hryniewicz, and P.-T. Ho, "Propagation loss in single-mode GaAs–AlGaAs microring resonators: measurement and model," *Journal of Lightwave Technology*, vol. 19, no. 11, pp. 1734–1739, 2001.
- [21] U. Gubler and C. Bosshard, "Molecular design for third-order nonlinear optics," *Polymer for Photonics Applications I*: Springer Berlin Heidelberg, 2002.
- [22] M. A. Newhouse, D. L. Weidman, and D. W. Hall, "Enhanced-nonlinearity single-mode lead silicate optical fiber," *Optics Letters*, vol. 15, no. 21, pp. 1185–1187, 1990.

- [23] B. L. Booth, "Low loss channel waveguide in polymers," *Journal of Lightwave Technology*, vol. 7, no. 10, pp. 1445–1453, 1989.
- [24] L. Eldada and L. W. Shacklette, "Advances in polymer integrated optics," *IEEE Journal of Selected Topics in Quantum Electronics*, vol. 6, no. 1, pp. 54–68, 2000.
- [25] L. Robitaille, C. L. Callender, and J. P. Noad, "Polymer waveguide devices for WDM applications," *Proceedings of SPIE*, vol. 3281, pp. 14–24, 1998.
- [26] W.-Y. Chen, R. Grover, T. A. Ibrahim, V. Van, W. N. Herman, and P.-T. Ho, "High-finesse laterally-coupled single-mode benzocyclobutene microring resonators," *IEEE Photonics Technology Letters*, vol. 16, no. 2, pp. 470–472, 2004.
- [27] J. K. S. Poon, Y. Huang, G. T. Paloczi, and A. Yariv, "Soft lithography replica molding of critically coupled polymer microring resonators," *IEEE Photonics Technology Letters*, vol. 16, no. 11, pp. 2496–2498, 2004.
- [28] C.-Y. Chao and L. J. Guo, "Polymer microring resonators fabricated by nanoimprint technique," *Journal of Vacuum Science & Technology B*, vol. 20, no.6, pp. 2862–2866, 2002.
- [29] J. Zhou, A. Pyayt, L. R. Dalton, J. Luo, A. K. Y. Jen, and A. Chen, "Photobleaching fabrication of microring resonator in a chromophore-containing polymer," *IEEE Photonics Technology Letters*, vol. 18, no. 21, pp. 2221–2223, 2006.
- [30] L. Li, W.-Y. Chen, T. N. Ding, W. N. Herman, P.-T. Ho, and J. T. Fourkas, "Microring resonators using multiphoton absorption polymerization,"

presented at Conference on Lasers and Electro-Optics (CLEO) 2007, Baltimore, MD, 2007.

- [31] A. J. Boyle and W. J. Blau, "Polymer waveguides for ultra-high speed optical signal processing devices," presented at Pacific Rim Conference on Lasers and Electro-Optics (CLEO/Pacific Rim) 2001, Chiba, Japan, 2001.
- [32] Y. Shi, C. Zhang, H. Zhang, J. H. Bechtel, L. R. Dalton, B. H. Robinson, W. H. Steier, "Low (sub-1-volt) halfwave voltage polymeric electro-optic modulators achieved by controlling chromophore shape," *Science*, vol. 288, no. 5463, pp. 119–122, 2000.
- [33] D. H. Park, J. W. Kang, J. D. Luo, T. D. Kim, A. K.-Y. Jen, C. H. Lee, and W. N. Herman, "Nonlinear ellipsometric analysis of poled organic glasses having very large electro-optic coefficients," *Proceedings of SPIE*, vol. 5935, pp. 157–168, 2005.
- [34] P. Rabiei, W. H. Steier, C. Zhang, and L. R. Dalton, "Polymer micro-ring filters and modulators," *Journal of Lightwave Technology*, vol. 20, no. 11, pp. 1968–1975, 2002.
- [35] D. Burdeaux, P. Townsend, J. Carr, and P. Garrou, "Benzocyclobutene (BCB) dielectrics for the fabrication of high density thin film multichip modules," *Journal of Electronic Materials*, vol. 19, no. 12, pp. 1357–1366, 1990.
- [36] Y.-H. So, P. Garrou, J.-H. Im, and D. M. Scheck, "Benzocyclobutene-based polymers for microelectronics," *Chemical Innovation*, vol. 31, no. 12, pp. 40–47, 2001.

- [37] C. F. Kane and R. R. Krchnavek, "Banzocyclobutene optical waveguides," *IEEE Photonics Technology Letters*, vol. 7, no. 5, pp.535–537, 1995.
- [38] P. P. Absil, J. V. Hryniewicz, B. E. Little, F. G. Johnson, and P.-T. Ho, "Vertically coupled microring resonators using polymer wafer bonding," *IEEE Photonics Technology Letters*, vol. 13, no. 1, pp.49–51, 2001.
- [39] H. A. Haus, *Waves and Fields in Optoelectronics*: Prentice-Hall, 1983.
- [40] J. E. Heebner and R. W. Boyd, "Enhanced all-optical switching by use of a nonlinear fiber ring resonator," *Optics Letters*, vol. 24, no. 12, pp.847–849, 1999.
- [41] P. P. Absil, J. V. Hryniewicz, B. E. Little, R. A. Wilson, L. G. Joneckis, and P.-T. Ho, "Compact microring notch filters," *IEEE Photonics Technology Letters*, vol. 12, no. 4, pp. 398–400, 2000.
- [42] <http://www.apollophoton.com/>, *Optical Waveguide Mode Solvers (OWMS) Suite*, ver. 1.21: Apollo Photonics.
- [43] <http://www.apollophoton.com/>, *Apollo Photonic Solutions Suite (APSS)*, ver. 2.03: Apollo Photonics.
- [44] C. R. Pollock, *Fundamentals of Optoelectronics*: Irwin, 1995.
- [45] F. P. Kapron, D. B. Keck, and R. D. Mauer, "Radiation losses in glass optical waveguides," *Applied Physics Letters*, vol. 17, no. 10, pp.423–425, 1970.
- [46] M. Heiblum and J. H. Harris, "Analysis of curved optical waveguides by conformal transformation," *IEEE Journal of Quantum Electronics*, vol. QE-11, no. 2, pp. 75–83, 1975.

- [47] W. Berglund and A. Gopinath, "WKB analysis of bend losses in optical waveguides," *Journal of Lightwave Technology*, vol. 18, no. 8, pp.1161–1166, 2000.
- [48] S. L. Chuang, *Physics of Optoelectronic Devices*: John Wiley & Sons, 1995.
- [49] P. B. Chinoy, "Reactive ion etching of benzocyclobutene polymer films," *IEEE Transactions on Component, Packaging, and Manufacturing Technology – Part C*, vol. 20, no. 3, pp. 199–206, 1997.
- [50] L. B. Soldano, F. B. Veerman, M. K. Smit, B. H. Verbeek, A. H. Dubost, and E.C. M. Pennings, "Planar monomode optical couplers based on multimode interference effects," *Journal of Lightwave Technology*, vol. 10, no. 12, pp. 1843–1850, 1992.
- [51] <http://www.rsoftdesign.com/>, *Fullwave*, ver. 4.0: RSoft Design Group.
- [52] B. E. Little, S. T. Chu, J. V. Hryniewicz, and P. P. Absil, "Filter synthesis for periodically coupled microring resonators," *Optical Letters*, vol. 25, no. 5, pp. 344–346, 2000.
- [53] A. Melloni, F. Morichetti, and M. Martinelli, "Optical slow wave structures," *Optics & Photonics News*, vol. 14, no. 11, pp. 44–48, 2003.
- [54] J. E. Heebner and R. W. Boyd, "'Slow' and 'fast' light in resonator-coupled waveguides," *Journal of Modern Optics*, vol. 49, no. 14/15, pp. 2629–2636, 2002.
- [55] J. E. Heebner, P. Chak, S. Pereira, J. E. Sipe, and R. W. Boyd, "Distributed and localized feedback in microresonator sequences for linear and nonlinear

- optics,” *Journal of the Optical Society of America B*, vol. 21, no. 10, pp. 1818–1832, 2004.
- [56] S. Pereira, P. Chak, and J. E. Sipe, “Gap-soliton switching in short microresonator structures,” *Journal of the Optical Society of America B*, vol. 19, no. 9, pp. 2191–2201, 2002.
- [57] B. E. Little, S. T. Chu, P. P. Absil, J. V. Hryniewicz, F. G. Johnson, D. Seiferth, D. Gill, V. Van, O. King, and M. Trakalo, “Very high-order microring resonator filters for WDM applications,” *IEEE Photonics Technology Letters*, vol. 16, no. 10, pp. 2263–2265, 2004.
- [58] J. K. S. Poon, L. Zhu, G. A. Derose, and A. Yariv, “Polymer microring coupled-resonator optical waveguides,” *Journal of Lightwave Technology*, vol. 24, no. 4, pp. 1843–1849, 2006.
- [59] R. Grover, V. Van, T. A. Ibrahim, P. P. Absil, L. C. Calhoun, F. G. Johnson, J. V. Hryniewicz, and P.-T. Ho, “Parallel-cascaded semiconductor microring resonators for high-order and wide-FSR filters,” *Journal of Lightwave Technology*, vol. 20, no. 5, pp. 900–905, 2002.
- [60] R. Grover, T. A. Ibrahim, S. Kanakaraju, L. Lucas, L. C. Calhoun, and P.-T. Ho, “A tunable GaInAsP–InP optical microring notch filter,” *IEEE Photonics Technology Letters*, vol. 16, no. 2, pp. 467–469, 2004.
- [61] P. Rabiei and W. H. Steier, “Tunable polymer double micro-ring filters,” *IEEE Photonics Technology Letters*, vol. 15, no. 9, pp. 1255–1257, 2003.

- [62] B. Corbett, "Spectral characteristics of single-In_{0.7}Ga_{0.3}As quantum-well microring lasers." *IEEE Photonics Technology Letters*, vol. 10, no. 1, pp. 3–5, 1998.
- [63] K. Amarnath, R. Grover, S. Kanakaraju, and P.-T. Ho, "Electrically pumped InGaAsP–InP microring optical amplifiers and lasers with surface passivation," *IEEE Photonics Technology Letters*, vol. 17, no. 11, pp. 2280–2282, 2005.
- [64] G. I. Stegeman and R. H. Stolen, "Waveguides and fibers for nonlinear optics," *Journal of Optical Society America B*, vol. 6, no. 4, pp. 652–662, 1989.
- [65] T. A. Ibrahim, W. Cao, Y. Kim, J. Li, J. Goldhar, P.-T. Ho, and C. H. Lee, "Lightwave switching in semiconductor microring devices by free carrier injection," *Journal of lightwave technology*, vol. 21, no. 12, pp. 2997–3003, 2003.
- [66] V. Van, T. A. Ibrahim, P. P. Absil, F. G. Johnson, R. Grover, and P.-T. Ho, "Optical signal processing using nonlinear semiconductor microring resonators," *IEEE Journal of Selected Topics in Quantum Electronics*, vol. 8, no. 3, pp. 705–713, 2002.
- [67] T. A. Ibrahim, V. Van, and P.-T. Ho, "All-optical time-division demultiplexing and spatial pulse routing with a GaAs/AlGaAs microring resonator," *Optics Letters*, vol. 27, no. 10, pp. 803–805, 2002.
- [68] T. A. Ibrahim, R. Grover, L.-C. Kuo, S. Kanakaraju, L. C. Calhoun, and P.-T. Ho, "All-optical AND/NAND Logic gates using semiconductor

- microresonators,” *IEEE Photonics Technology Letters*, vol. 15, no. 10, pp. 1422–1424, 2003.
- [69] T. A. Ibrahim, K. Amarnath, L. C. Kuo, R. Grover, V. Van, and P.-T. Ho, “Photonic logic NOR gate based on two symmetric microring resonators,” *Optics Letters*, vol. 29, no. 23, pp. 2779–2781, 2004.
- [70] H.-Y. Ng, M. R. Wang, D. Li, X. Wang, J. Martinez, R. R. Panepucci, and K. Pathak, “1×4 wavelength reconfigurable photonic switch using thermally tuned microring resonators fabricated on silicon substrate,” *IEEE Photonics Technology Letters*, vol. 19, no. 9, pp. 704–706, 2007.
- [71] <http://www.metricon.com/>, *The Prism Coupler Model 2010*, Metricon.
- [72] H. M. Gibbs, *Optical Bistability: Controlling Light with Light*: Academic Press, 1985.
- [73] Y. R. Shen, *The Principles of Nonlinear Optics*: John Wiley & Sons, 1984.
- [74] R. W. Boyd, *Nonlinear Optics*: Academic Press, 1992.
- [75] R. Ushigome, M. Fujita, A. Sakai, T. Baba, and Y. Kokubun, “GaInAsP microdisk injection laser with benzocyclobutene polymer cladding and its athermal effect,” *Japanese Journal of Applied Physics*, vol. 41, no. 11A, pp. 6364–6369, 2002.
- [76] C. Hu, M. Kiene, and P. S. Ho, “Thermal conductivity and interfacial thermal resistance of polymeric low k films,” *Applied Physics Letters*, vol. 79, no. 25, pp. 4121–4123, 2001.
- [77] <http://www.hbcnpnetbase.com/>, *Handbook of Chemistry and Physics*, 87th ed.: Taylor & Francis CRC Press.

- [78] S.-Y. Tseng, W. Cao, Y.-H. Peng, J. M. Hales, S.-H. Chi, J. W. Perry, S. R. Marder, C. H. Lee, W. N. Herman, and J. Goldhar, “Measurement of complex $\chi^{(3)}$ using degenerate four-wave mixing with an imaged 2-D phase grating,” *Optics Express*, vol. 14, no. 19, pp. 8737–8744, 2006.